

The rupture extent of low frequency earthquakes near Parkfield, CA

Jessica C. Hawthorne (Department of Earth Sciences, University of Oxford, Oxford, UK)
Amanda M. Thomas (Department of Earth Sciences, University of Oregon, Oregon, USA)
Jean-Paul Ampuero (Université Côte d'Azur, IRD, CNRS, Observatoire de la Côte d'Azur, Géoazur,
France; California Institute of Technology, Seismological Laboratory, Divisional of Geological and
Planetary Sciences, Pasadena, CA, USA)

Manuscript accepted for publication in *Geophysical Journal International*, doi: 10.1093/gji/ggy429

Abstract

The low frequency earthquakes (LFEs) that constitute tectonic tremor are often inferred to be slow: to have durations of 0.2 to 0.5 s, a factor of 10 to 100 longer than those of typical M_W 1-2 earthquakes. Here we examine LFEs near Parkfield, CA in order to assess several proposed explanations for LFEs' long durations. We determine LFE rupture areas and location distributions using a new approach, similar to directivity analysis, where we examine how signals coming from various locations within LFEs' finite rupture extents create differences in the apparent source time functions recorded at various stations. We use synthetic ruptures to determine how much the LFE signals recorded at each station would be modified by spatial variations of the source-station travel time within the rupture area given various possible rupture diameters, and then compare those synthetics with the data. Our synthetics show that the methodology can identify inter-station variations created by heterogeneous slip distributions or complex rupture edges, and thus lets us estimate LFE rupture extents for unilateral or bilateral ruptures. To obtain robust estimates of the sources' similarity across stations, we stack signals from thousands of LFEs, using an empirical Green's function approach to isolate the LFEs' apparent source time functions from the path effects. Our analysis of LFEs in Parkfield implies that LFEs' apparent source time functions are similar across stations at frequencies up to 8 to 16 Hz, depending on the family.

The inter-station coherence observed at these relatively high frequencies, or short wavelengths (down to 0.2 to 0.5 km), suggest that LFEs in each of the 7 families examined occur on asperities. They are clustered in patches with sub-1-km diameters. The individual LFEs' rupture diameters are estimated to be smaller than 1.1 km for all families, and smaller than 0.5 km and 1 km for the two shallowest families, which were previously found to have 0.2-s durations. Coupling the diameters with the durations suggests that it is possible to model these M_W 1-2 LFEs with earthquake-like rupture speeds: around 70% of the shear wave speed. However, that rupture speed matches the data only at the edge of our uncertainty estimates for the family with highest coherence. The data for that family are better matched if LFEs have rupture velocities smaller than 40% of the shear wave speed, or if LFEs have different rupture dynamics. They could have long rise times, contain composite sub-ruptures, or have slip distributions that persist from event to event.

1 Introduction

Tectonic tremor is a long-duration seismic signal, best observed at frequencies between 1 and 10 Hz (e.g., *Obara, 2002; Rogers and Dragert, 2003; Payero et al., 2008; Peterson and Christensen, 2009; Rubinstein et al., 2009; Fry et al., 2011*). It is thought to consist of numerous small low frequency earthquakes, or LFEs (*Shelly et al., 2006, 2007; Wech and Creager, 2007; Brown et al., 2009*). LFEs are often inferred to have magnitudes between M_W 1 and 2.5 but to have corner frequencies of a few Hz, a factor of 10 to 100 times smaller than corner frequencies observed for “normal” M_W 1-2.5 earthquakes (*Fletcher and McGarr, 2011; Zhang et al., 2011; Bostock et al., 2017*). LFEs are found to have durations around 0.2 seconds in Parkfield (*Thomas et al., 2016*) and around 0.5 s in Cascadia (*Bostock et al., 2015*), which are a factor of 10 to 100 longer than “normal” M_W 1-2.5 earthquakes.

1.1 Potential Causes of LFEs’ Long Durations

The durations of normal earthquakes are determined by their spatial extent: by how long it takes the rupture to progress across the earthquake area. Models and observations suggest that earthquake ruptures usually progress at speeds of 2 to 3 km/s, or 60 to 95% of the shear wave speed V_s (*Kanamori and Brodsky, 2004; McGuire, 2004; Madariaga, 2007; Seekins and Boatwright, 2010; Taira et al., 2015; Folesky et al., 2016; Ye et al., 2016; Melgar and Hayes, 2017; Chounet et al., 2018*). Earthquakes’ durations can thus be roughly estimated by dividing their rupture lengths by the shear wave speed. If LFEs, like normal earthquakes, rupture at speeds close to the shear wave speed, their long durations could indicate that LFEs have unusually large lengths given their moment: perhaps 0.7 to 1.5 km. In this scenario, LFEs would have lower stress drops than normal earthquakes: 0.1 to 10 kPa, but they could otherwise be governed by the same physical processes. LFEs could be driven by unstable frictional sliding, and their slip speeds could be limited by the energy that they dissipate via seismic waves (e.g., *Rice, 1980; Kanamori and Brodsky, 2004*).

However, it is also possible that seismic wave generation has minimal impact on LFE dynamics and that LFEs are governed by different fault zone processes. LFEs’ slip rates may be limited by a spatial constraint or by a speed-limiting frictional rheology (e.g., *Liu and Rice, 2005, 2007; Shibazaki and Shimamoto, 2007; Rubin, 2008; Segall et al., 2010; Skarbek et al., 2012; Fagereng et al., 2014; Yabe and Ide, 2017*). For instance, LFEs could occur on faults with a velocity-strengthening rheology, which inhibits increases in slip rate. The brief slip rate increases seen in LFEs could result from imposed local stress concentrations, perhaps created by the creep fronts of large slow slip events (e.g., *Perfettini and Ampuero, 2008; Rubin, 2009*). Alternatively, LFEs could occur on faults with a more complex rheology, which encourages initial increases in slip rate but inhibits slip rates higher than some cutoff speed. Such rheologies are commonly proposed for slow slip events and may be created by shear-induced dilatancy or by a minimum asperity size (e.g., *Shibazaki and Iio, 2003; Shibazaki and Shimamoto, 2007; Liu et al., 2010; Segall et al., 2010; Hawthorne and Rubin, 2013; Poulet et al., 2014*). The possibility that LFEs are small versions of slow slip events is intriguing because slip rates vary widely from slow slip to tremor (*Ide et al., 2007, 2008; Aguiar et al., 2009; Gao et al., 2012; Ide and Yabe, 2014; Hawthorne and Bartlow, 2018*). Several of the processes proposed to govern slow slip would have difficulty producing such a wide range of slip rates (e.g., *Liu and Rice, 2005, 2007; Shibazaki and Shimamoto, 2007; Hawthorne and Rubin, 2013; Fagereng et al., 2014; Veveakis et al., 2014*). If LFE slip rates are

80 limited primarily by frictional resistance to shear and not by seismic wave radiation, LFEs need not
81 rupture across the fault at speeds close to the shear wave speed. They could rupture more slowly
82 and have diameters far smaller than 1 km despite their 0.2-s durations.

83 LFEs could also have small rupture diameters if their 0.2-s durations and low corner frequencies
84 are actually apparent values, not true values. LFEs could be “normal” M_W 1-2.5 earthquakes, with
85 0.01-s durations and 10-m rupture diameters. They may appear to be dominated by low-frequency
86 signals only because their high-frequency signals are attenuated when they pass through a highly
87 damaged fault zone or through a region of high pore fluid pressure (Gomberg *et al.*, 2012; Bostock
88 *et al.*, 2017). Regions of high pore pressure or increased attenuation are frequently identified near
89 the slow slip region (Audet *et al.*, 2009; Song *et al.*, 2009; van Avendonk *et al.*, 2010; Kato *et al.*,
90 2010; Fagereng and Diener, 2011; Kitajima and Saffer, 2012; Nowack and Bostock, 2013; Yabe
91 *et al.*, 2014; Saffer and Wallace, 2015; Audet and Schaeffer, 2018), though we note that any regions
92 with attenuation strong enough to produce tremor’s frequency content might have to be localized
93 into patches. Earthquakes do occur below the tremor-generating region, and some of them show
94 higher-frequency signals than tremor (Seno and Yamasaki, 2003; Shelly *et al.*, 2006; Bell *et al.*,
95 2010; Kato *et al.*, 2010; Ohta and Ide, 2011; Gomberg *et al.*, 2012; Bostock *et al.*, 2017).

96 **1.2 Potential Role of Tremor Asperities**

97 Tremor is often patchily distributed along the plate interface; it is densely concentrated in some
98 regions but appears absent in others (e.g., Payero *et al.*, 2008; Maeda and Obara, 2009; Walter
99 *et al.*, 2011; Ghosh *et al.*, 2012; Armbruster *et al.*, 2014). Some observations and models suggest
100 that tremor occurs only on a set of tremor-generating asperities (e.g., Ariyoshi *et al.*, 2009; Ando
101 *et al.*, 2010; Shelly, 2010b; Nakata *et al.*, 2011; Ando *et al.*, 2012; Sweet *et al.*, 2014; Veedu and
102 Barbot, 2016; Chestler and Creager, 2017a,b; Luo and Ampuero, 2017). Such asperities may also
103 be suggested by the success of template matching approaches to tremor identification, in which
104 LFEs are detected and grouped into families according to waveform similarity. Each LFE family
105 could reflect an individual tremor asperity (Shelly *et al.*, 2007; Brown *et al.*, 2008; Bostock *et al.*,
106 2012; Frank *et al.*, 2013; Kato, 2017; Shelly, 2017). However, the family grouping could also result
107 from more gradual variations in the path effects. LFEs located more than 1 or a few km away from
108 each other may be grouped into distinct families simply because the path effects vary significantly
109 on several-km length scales, so that well-separated LFEs give rise to distinct seismograms.

110 A few studies have provided further indications that at least some LFE families are created
111 by clusters of tremor. Sweet *et al.* (2014) relocated LFEs within an isolated family in Cascadia
112 and found that they clustered within a 1-km-wide patch. Chestler and Creager (2017b) relocated
113 LFEs within around 20 families in Cascadia and found that LFEs cluster within 1 to 2-km-wide
114 patches that are often separated by > 5 -km-wide areas with few to no LFEs, or at least few to no
115 detected LFEs. Tremor-generating asperities are also suggested by the highly repetitive recurrence
116 intervals of one isolated LFE family near Parkfield, CA. The consistent rupture intervals suggest
117 that the LFEs could be repeating similar ruptures of a particular asperity (Shelly, 2010b; Veedu
118 and Barbot, 2016). Repetitive LFE rupture is also suggested by LFE moments and durations that
119 vary little from event to event, creating exponential amplitude distributions (Watanabe *et al.*, 2007;
120 Shelly and Hardebeck, 2010; Chamberlain *et al.*, 2014; Sweet *et al.*, 2014; Bostock *et al.*, 2015;
121 Chestler and Creager, 2017a), though it is also possible that each LFE ruptures only a portion of a
122 tremor-generating asperity. The total slip on an LFE patch could result from a range of ruptures of

123 different types, as well as some aseismic slip (*Chestler and Creager, 2017a*).

124 **1.3 Analysis to Be Presented**

125 In this study, we further assess whether small asperities control tremor generation and whether
126 LFEs are governed by earthquake-like or slow slip rheologies. We determine the rupture extents
127 of LFEs in seven families near Parkfield, CA and place upper bounds on the spatial distribution
128 of LFEs in each family and on the average LFE rupture area. In order to obtain these bounds, we
129 will introduce a new coherence-based approach, which can be thought of as a version of directivity
130 analysis that we have modified so that we can combine data from thousands of LFEs which may
131 rupture unilaterally or bilaterally (e.g. *Mueller, 1985; Mori and Frankel, 1990; Got and Fréchet,*
132 *1993; Velasco et al., 1994; Lengliné and Got, 2011; Wang and Rubin, 2011; Kane et al., 2013*). We
133 examine how signals coming from various locations within LFEs’ finite rupture areas can produce
134 complex apparent source time functions (ASTFs) that vary from station to station. We quantify the
135 ASTF variation as a function of frequency, or seismic wavelength, in order to determine the LFE
136 rupture area.

137 We qualitatively explain how the ASTFs’ frequency-dependent variability should reflect LFEs’
138 rupture extents in section 2. In section 3, we present our approach in more detail. We describe
139 how we can isolate the ASTFs from observed seismograms using an empirical Green’s function
140 approach and then describe how we can quantify the ASTFs’ coherence among LFEs and among
141 stations. In sections 4 and 5, we analyze ASTF coherence for individual LFEs near Parkfield and
142 then average over thousands of LFEs to obtain well-resolved estimates of inter-station coherence as
143 a function of frequency. For comparison, we also compute ASTF coherence for a suite of synthetic
144 LFEs with a range of diameters and rupture velocities (section 6). Finally, in sections 7 and 8,
145 we compare the data with the synthetics to determine which rupture areas are plausible and which
146 types of LFEs could match the observations.

147 **2 Premise: Mapping Inter-Station Similarity to Rupture Area**

148 In order to estimate LFE areas, we note that seismic waves generated at a range of locations
149 throughout the source region require different amounts of time to travel to the various stations.
150 For instance, in the rupture illustrated in Figure 1d, seismic waves generated by the high-slip as-
151 perity marked in red arrive earliest at the NW station (left) because the asperity is located in the
152 northwestern half of the rupture. But waves generated at the blue asperity, located farther SE
153 (right), arrive first at the SE station. The time-shifted signals give rise to apparent source time
154 functions (ASTFs) that differ among the recording stations, as seen in Figure 1a-c.

155 If we assume that Earth structure is relatively uniform within the source region, we may account
156 for the travel time variations by modeling the observed seismograms d_k in terms of station-specific
157 apparent source time functions s_k . At each station k ,

$$\hat{d}_k(\omega) = \hat{s}_k(\omega)\hat{g}_k(\omega). \quad (1)$$

158 Here g_k is an average Green’s function for the source area, and \hat{d}_k , \hat{s}_k , and \hat{g}_k are the Fourier
159 coefficients of d_k , s_k , and g_k , respectively.

160 The ASTFs s_k can be computed by integrating time-shifted versions of the slip rate functions
 161 over the rupture area. If $g_k(t)$ is taken as the Green's function for a reference location x_0 , and if
 162 $\dot{\delta}(x, t)$ is the slip rate as a function of location x and time t , and $\Delta t_k(x)$ is the source-station travel
 163 time for a signal generated at location x ,

$$s_k(t) = \int_{\text{rupture area}} \dot{\delta}(x, t - \Delta t_k(x) + \Delta t_k(x_0)) dA. \quad (2)$$

164 The coloring in Figure 1 shows how the three slip asperities shown contribute to ASTFs that differ
 165 among stations located to the northwest, southeast, and above the earthquake. Note that the asperities
 166 create differences at all three stations even though the earthquake ruptures radially out from
 167 the center point.

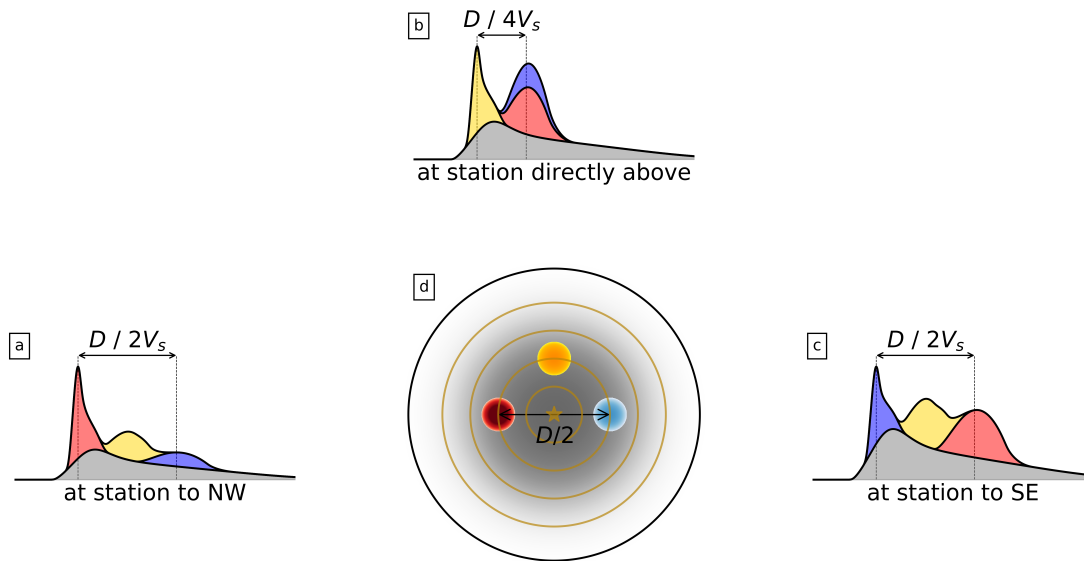


Figure 1: (a-c) ASTFs observed at 3 stations due to rupture of the slip distribution illustrated with gray and colored shading in panel (d). Rupture progresses outward from the center and moves through 3 high-slip asperities of varying magnitude, illustrated with colored circles. The asperities generate seismic waves which require different amounts of time to travel to the stations, giving rise to the various colored peaks in the ASTFs. Note that the timing of the asperity-created peaks varies among the stations by up to $D/2V_s$: by half the rupture diameter divided by the shear wave speed.

168 There is, however, a limit to the ASTF differences. The spatially variable source-station travel
 169 time may shift peaks in this earthquake's source time function by only a limited amount: up to
 170 D/V_s , the rupture diameter D divided by the seismic wavespeed V_s . Thus we can see differences
 171 in the ASTFs only if we examine their short-period signal. If we examine ASTFs at periods much
 172 longer than D/V_s , the travel time shifts will be a small fraction of the period, and the ASTFs
 173 will be roughly the same at all stations. Synthetic rupture models described in section 6 show
 174 that ASTFs are similar among stations at periods longer than 0.45 to $1.4D/V_s$. Here the range
 175 of limiting periods results from the earthquakes' other rupture parameters, but we note that the

176 limiting periods depend primarily on the diameter divided by seismic wave speed V_s , not on the
 177 diameter divided by the LFEs' rupture speed V_r . We will thus be able to use the ASTFs' frequency-
 178 dependent similarity to estimate LFE rupture extents without making restrictive assumptions about
 179 LFE rupture dynamics.

180 3 Quantifying Coherence Across Events and Stations

181 3.1 Removing the Path Effect

182 In order to examine ASTFs, we must first isolate them from the observed seismograms. To do so,
 183 we use an empirical Green's function approach similar to that of *Hawthorne and Ampuero (2017)*
 184 and compare each LFE's seismograms with a template event created via stacking (a variant on, e.g.,
 185 *Mueller, 1985; Mori and Frankel, 1990; Velasco et al., 1994; Hough, 1997; Prieto et al., 2004;*
 186 *Baltay et al., 2010; Kwiatek et al., 2011; Uchide et al., 2014*). Both the seismograms d_{jk} of the
 187 individual LFEs j and the seismograms d_{tk} of the templates t can be approximated as convolutions
 188 of ASTFs s_{jk} or s_{tk} and Green's functions g_k , so that, in the frequency domain,

$$\hat{d}_{jk}(\omega) = \hat{s}_{jk}(\omega)\hat{g}_k(\omega). \quad (3)$$

189 To isolate the ASTFs from the Green's functions, we compute the normalized cross-spectrum
 190 \hat{x}_{jk} of the individual and template records:

$$\hat{x}_{jk} = \frac{\hat{d}_{jk}\hat{d}_{tk}^*}{|\hat{d}_{tk}^*|^2} = \frac{\hat{s}_{jk}\hat{s}_{tk}^*|\hat{g}_k|^2}{|\hat{s}_{tk}|^2|\hat{g}_k|^2} = \frac{\hat{s}_{jk}\hat{s}_{tk}^*}{|\hat{s}_{tk}|^2}, \quad (4)$$

191 where $*$ denotes the complex conjugate, and we have omitted the frequency indexing for readabil-
 192 ity. In the second equality, we have assumed that the template LFE has the same Green's functions
 193 as the individual event. In this case, the path effects cancel out, and we are left with a function that
 194 depends on the relative amplitudes and phases of the individual and template ASTFs. Note that we
 195 always normalize by the template amplitude, as this will allow us to stack ASTFs from thousands
 196 of LFEs, and to use the cross-spectra \hat{x}_{jk} to examine how ASTFs' amplitudes and phases vary
 197 among LFEs j and stations k .

198 3.2 ASTF Energy: Direct and Inter-Station Coherence

199 As a first step in our analysis, we ignore inter-station variations, and simply examine how much
 200 LFE source time functions vary from event to event. We assess the similarity between the individ-
 201 ual and template ASTFs by computing the directly coherent power for each LFE j :

$$P_d = \frac{1}{N} \sum_{k=1}^N a_{jk}^2 [\text{Re}(\hat{x}_{jk})]^2 \text{sgn}[\text{Re}(\hat{x}_{jk})] \quad (5)$$

$$= \frac{1}{N} \sum_{k=1}^N a_{jk}^2 \left[\text{Re} \frac{\hat{s}_{jk}\hat{s}_{tk}^*}{|\hat{s}_{tk}|^2} \right]^2 \text{sgn}[\text{Re}(\hat{s}_{jk}\hat{s}_{tk}^*)]. \quad (6)$$

202 Here the coefficients a_{jk} represent a weighting of the LFE records, which we will use to down-
 203 weight noisy seismograms (section 4.3).

204 The equality in equation (6) assumes that the individual LFE and the template have the same
 205 path effects. If the individual and template LFEs have the same path effects, and in addition have
 206 similar and well-aligned ASTFs \hat{s}_{jk} and \hat{s}_{tk} , so that the value $\hat{s}_{jk}\hat{s}_{tk}^*$ in equation (6) is real and
 207 positive, then the directly coherent power P_d will be positive. Its amplitude will be determined by
 208 the relative power of the individual and template ASTFs.

209 The relative ASTF power also determines the amplitude of the inter-station coherent power P_c .
 210 With this power calculation, we seek to ignore ASTF variations across events, and instead assess
 211 the ASTFs' similarity across stations. So we compute (see section S1 for computational details)

$$P_c = \frac{2}{N(N-1)} \sum_{k=1}^N \sum_{l=k+1}^N a_{jk}a_{jl} \operatorname{Re}(\hat{x}_{jk}\hat{x}_{jl}^*) \quad (7)$$

$$= \frac{2}{N(N-1)} \sum_{k=1}^N \sum_{l=k+1}^N a_{jk}a_{jl} \operatorname{Re} \frac{(\hat{s}_{jk}\hat{s}_{jl}^*)(\hat{s}_{tk}^*\hat{s}_{tl})}{|\hat{s}_{tk}|^2|\hat{s}_{tl}|^2}, \quad (8)$$

212 where the second equality again assumes common path effects and where the summation is across
 213 pairs of the N stations, indexed k and l . As noted in section 2, the ASTFs are expected to be the
 214 same for all stations if the period being considered with these Fourier coefficients is long compared
 215 with D/V_s , the intra-source seismic wave travel time. If the ASTFs are the same across stations at
 216 the period of interest, we will have $\hat{s}_{jk} = \hat{s}_{jl}$ and $\hat{s}_{tk} = \hat{s}_{tl}$, so that all three of $\hat{s}_{jk}\hat{s}_{jl}^*$, $\hat{s}_{tk}^*\hat{s}_{tl}$, and P_c
 217 are real and positive.

218 P_d and P_c thus give us estimates of the direct or inter-station coherent power of an LFE, as
 219 normalized by the template power. However, we can obtain a more interpretable normalization if
 220 we also estimate the full template-normalized LFE power, including any incoherent contributions:

$$P_l = \frac{1}{N} \sum_{k=1}^N a_{jk}^2 |\hat{x}_{jk}|^2 \quad (9)$$

$$= \frac{1}{N} \sum_{k=1}^N a_{jk}^2 \frac{|\hat{s}_{jk}|^2}{|\hat{s}_{tk}|^2}. \quad (10)$$

221 We will use the LFE power P_l to normalize P_d and P_c and compute the fraction of the power that
 222 is coherent across events and stations.

223 4 Calculating Powers of Parkfield LFEs

224 When we extract the coherent and incoherent powers of LFEs near Parkfield, we will also have to
 225 estimate and remove the power contributed by noise, and we will have to average over thousands
 226 of LFEs to obtain well-resolved powers. To begin, we describe the LFE catalog and seismic data
 227 (section 4.1) and create templates for seven LFE families (section 4.2). Then we demonstrate our
 228 approach by estimating template-normalized powers for an individual LFE (section 4.3). Finally,
 229 we average the powers over the LFEs in each family (section 5).

230 **4.1 Data and LFE Families**

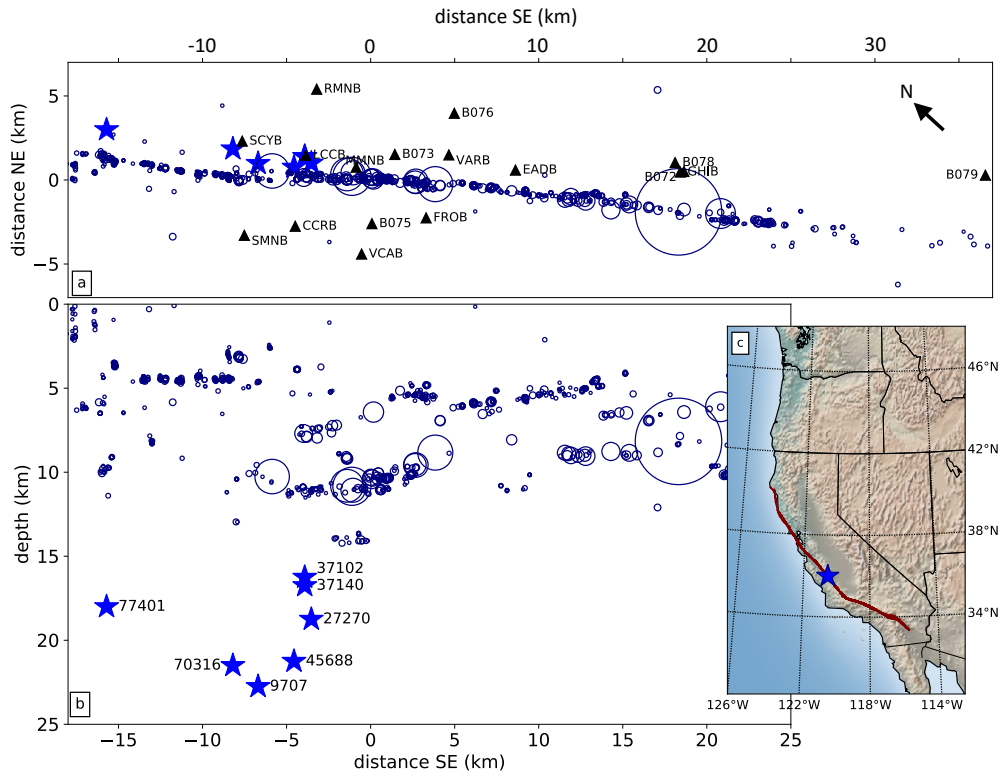


Figure 2: (a) Map view and (b) depth section of the LFE families (blue stars), local $M > 2.5$ earthquakes (circles), and the HRSN and PBO seismic stations used (triangles). Earthquake sizes are scaled to the radii expected for 3-MPa stress drops, and locations are taken from the NCSN catalog and the relocations of *Waldhauser* (2009).

231 The LFEs considered here occurred between 2006 and 2015 at depths of 16 to 23 km near
 232 Parkfield, CA (see Figure 2). They were identified via cross-correlation by *Shelly* (2017) as part
 233 of his 15-year tremor catalog and are grouped into seven families numbered 37140, 37102, 70316,
 234 27270, 45688, 77401, and 9707, with 2500 to 8300 LFEs in each family (see also *Shelly et al.*
 235 (2009); *Shelly and Hardebeck* (2010)). LFEs in families 37140 and 37102 were examined by
 236 *Thomas et al.* (2016) and found to have best-fitting source durations of 0.19 and 0.22 s, respec-
 237 tively. We use LFE seismograms from 17 borehole seismic stations in the Berkeley HRSN (High
 238 Resolution Seismic Network) and in the PBO (Plate Boundary Observatory) network. Since this
 239 analysis relies on high-quality records of small LFEs, we correct the data for some errors identified
 240 by *Shelly* (2017). We have also gone through the data from each station and channel and discarded
 241 weeks- to years-long intervals where the LFE amplitudes vary more strongly than usual from event
 242 to event, as these intervals likely have larger-than-average noise.

243 **4.2 Stacked LFE Templates**

244 For each LFE family, we create a low-noise template by averaging the LFE records for each chan-
 245 nel. We bandpass filter the LFE seismograms from 2 to 30 Hz, normalize them by their maximum

246 values, and then average, weighting each record by the station-averaged cross-correlation coeffi-
 247 cient obtained by *Shelly* (2017). Then we rescale these normalized stacks so that their amplitudes
 248 match the amplitudes of individual records, as described in section S2. We iterate the stack four
 249 times to be sure that the stacks’ amplitudes are stable and to improve the signal to noise ratio by
 250 of order 10%. In each iteration, we discard records with very small or unusual amplitudes (for
 251 details see section S2).

252 We estimate the signal to noise ratio of the stacks using a 3-second window starting just before
 253 the S arrival. We keep only the stacks which have average amplitude spectra at least 3 times larger
 254 than the noise in the 2 to 10 Hz band. The procedure leaves us with 16 to 29 well-resolved template
 255 seismograms for each LFE family, observed on the two horizontal components of 9 to 16 stations.
 256 Some templates are shown in Figure 3a, and the whole set of templates is shown Figures S1 to S7.

257 4.3 Coherent and Total Powers for One LFE

258 We will use the obtained templates to remove the Green’s functions from individual LFE records,
 259 so that we can probe the LFEs’ ASTFs. To prepare, we realign each LFE’s origin time to better
 260 match the template, as poor alignment can reduce the direct coherence P_d . We bandpass filter to 2
 261 to 5 Hz, cross-correlate to obtain a preferred shift at each station, and then shift the seismograms
 262 of all stations by the median shift.

263 Next, we remove the path effects to facilitate the power calculations. We extract 3-second-long
 264 segments of the template seismograms, starting just before the S arrival, and cross-correlate the
 265 segments with the individual LFE records. The individual LFE records are truncated 0.2 seconds
 266 before the S arrival to reduce contamination by the P arrival, but they are not truncated after the
 267 S wave. We average the cross-correlations over the available channels at each station.

268 Cross-correlations obtained for one LFE are illustrated in Figure 3b. The cross-correlations are
 269 often roughly but not entirely symmetric, suggesting that the individual and template LFEs have
 270 slightly different source time functions. The asymmetry is also apparent in the non-zero phases of
 271 the cross-correlations’ Fourier coefficients, which are equal to the phases of the normalized cross-
 272 spectra \hat{x}_{jk} (equation (4), Figure 3c). To estimate the \hat{x}_{jk} , we first extract a 6-second portion of the
 273 cross-correlations, multiply by a Slepian taper concentrated at frequencies lower than 0.4 Hz, and
 274 compute the Fourier transform (*Thomson*, 1982). Then we normalize; we divide by the Fourier
 275 transform of the template seismograms’ autocorrelation, computed via the same procedure.

276 We use the cross-spectra \hat{x}_{jk} to compute the power that is directly coherent (P_d , equation (5))
 277 and coherent among stations (P_c , equation (7)) and plot them in yellow and red in Figure 3d.
 278 The total power P_t in the template-normalized cross-correlation is also computed, following equa-
 279 tion (9), and is plotted in green. However, a significant fraction of this total power comes from
 280 noise, not from the LFE signal. To estimate the noise contribution, we cross-correlate the template
 281 seismograms with data from noise intervals starting 8 seconds before the S arrivals. We compute
 282 the power (P_n) in those noise correlations, again following equation (9), and plot it in gray in Fig-
 283 ure 3d. Finally, we subtract the noise power P_n from the total power P_t to determine the power
 284 contributed by the LFE (P_l , blue in Figure 3d).

285 In all the power calculations, we use weightings a_{jk} equal to one divided by the standard
 286 deviation of the 2 to 30-Hz filtered waveform, as computed in the four seconds ending 0.5 s before
 287 the LFE S arrival. This weighting reduces the importance of seismograms with large noise and
 288 allows us to better identify the LFEs’ coherence. Note that uniform weightings ($a_{jk} = 1$) would

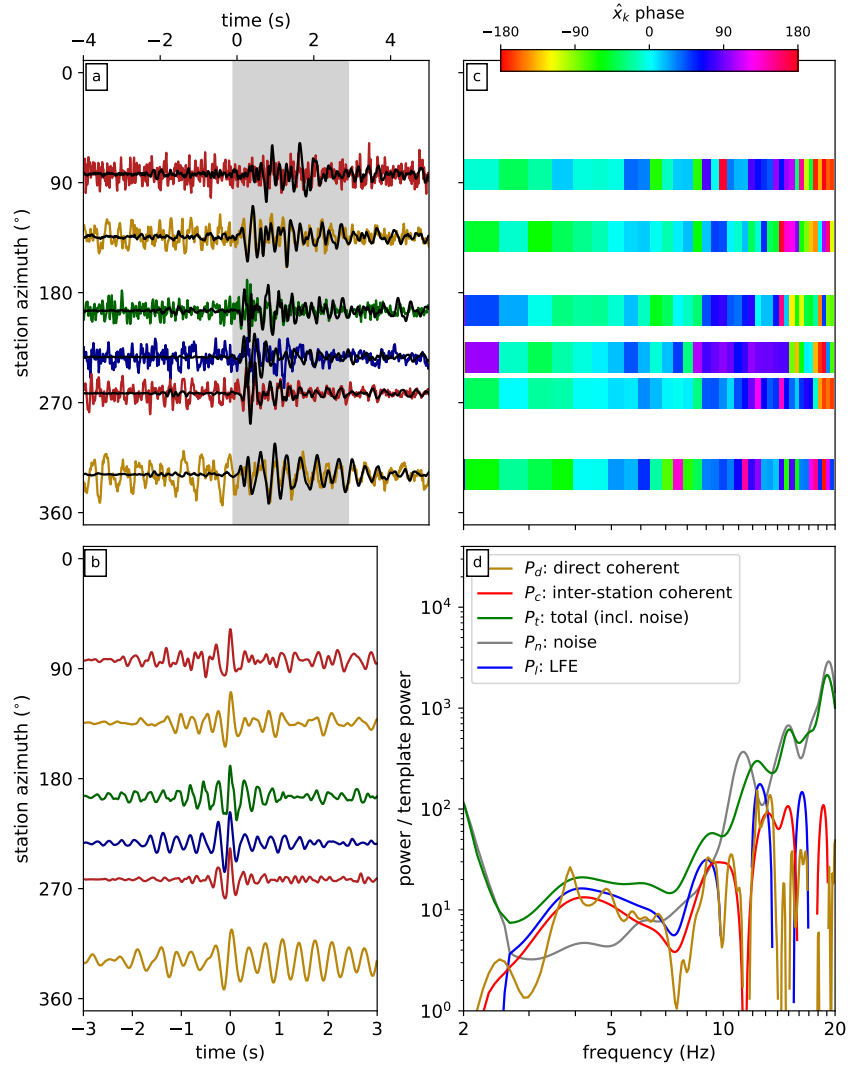


Figure 3: (a) Some of the template seismograms (black) for family 37102 along with seismograms observed for one LFE (color). Traces are organized according to the station’s azimuth relative to the LFE and are scaled to their maximum value. The gray shading indicates the portion of the template that is correlated with the individual observations. (b) Cross-correlations of the observed seismograms with the template. (c) Phase of the cross-spectra \hat{x}_k : of the Fourier coefficients of the cross-correlations in panel b. (d) Yellow, red, and green curves: P_d , P_c , and P_t —the coherent and total template-normalized powers from the LFE interval. Gray: P_n —the noise power, computed in an interval without the LFE. Blue: $P_l = P_t - P_n$ —the power likely contributed by the LFE. Note that with just this one LFE, it is not practical to interpret the relative values of the coherent and total powers.

289 result in lower coherence because a larger fraction of calculated powers would be contributed by
 290 noise, which is incoherent among stations. We choose weightings a_{jk} that depend on the signal
 291 between 4.5 and 0.5 s before the S arrival because these a_{jk} provide reasonable estimates of the
 292 noise, but they do not bias any of the power calculations, as all of the power in P_t , P_c , and P_d
 293 comes from after 0.2 s before the S arrival and almost all of the subtracted noise power P_n comes
 294 from more than 5 seconds before the S arrival. Note that the P-wave signal is small enough to be
 295 negligible. It never contributes more than a few percent of the power in the 4 s before the S arrival.

296 In an ideal scenario, we would now interpret the powers estimated for this LFE, and compare
 297 the coherent powers P_d and P_c with the LFE power P_l . However, for this and other individual
 298 LFEs, the powers are too poorly resolved to allow direct interpretation. In Figure 3d, the ratios
 299 P_d/P_l and P_c/P_l vary by tens of percent among the frequencies but show no systematic trend, and
 300 there is further variation if we use different subsets of the stations. So in the next section, we will
 301 average the powers over several thousand LFEs to obtain well-resolved and stable coherent power
 302 fractions.

303 5 Results: Event-Averaged Coherent and Incoherent Powers

304 To estimate P_c , P_d , P_t , and P_n for a given family of LFEs, we compute the powers for each event
 305 in the family and then average. However, some LFE records have exceptionally large noise, so
 306 we check the signals' amplitudes before the calculation and discard records when the S arrival or
 307 the preceding noise interval has standard deviation that differs by more than a factor of 10 from
 308 that channel's median. This record selection, coupled with data availability, leaves us with 860 to
 309 4220 LFEs per family which have template-normalized powers computed from at least 5 stations.

310 Figure 4a shows the summed coherent and total powers obtained from 2000 LFEs in fam-
 311 ily 37140, one of the two families with duration estimates from *Thomas et al. (2016)*. The shading
 312 indicates 95% uncertainty ranges on the powers, obtained by bootstrapping the LFEs included in
 313 the summation. All of the template-normalized powers increase with frequency, suggesting that
 314 the high-frequency template power is damped relative to a typical LFE. The stacks' high-frequency
 315 signal may be averaged out by stacking if LFEs are more different at higher frequencies or if the
 316 LFE timing is not accurate enough to allow coherent stacks at higher frequencies. The stacking
 317 effectively creates a template LFE which has slightly broader and simpler ASTFs (*Royer and Bo-*
 318 *stock, 2014*). This ASTF modification will reduce the direct coherence between the template and
 319 the individual LFEs P_d/P_l . However, smoothing the template ASTF in the same way at all stations
 320 should not affect P_c , as P_c is independent of inter-event ASTF differences. The ASTF averaging
 321 should reduce the inter-station coherence P_c/P_l only if the stacks' constituent LFEs are distributed
 322 in space, so that the station-dependent source-station arrival times vary among the LFEs. Stacking
 323 the shifted signals of such distributed LFEs would smooth the templates' ASTFs differently at
 324 different stations and could lead to reduced P_c/P_l .

325 We compute the coherent power fractions P_d/P_l and P_c/P_l for all 7 families and plot the
 326 results in Figure 4b-h. For family 37140 (panel b), the direct coherence P_d/P_l is larger than 0.8
 327 at frequencies of 2 to 4 Hz, suggesting that most 0.2-second-long LFE source time functions are
 328 similar when viewed at these frequencies. We should note, however, that P_d/P_l may be slightly
 329 higher than its true value in this range because we allowed for an LFE origin time shift using data
 330 in the 2 to 5-Hz range. P_d/P_l decreases at higher frequencies, falling below 0.6 at a frequency of

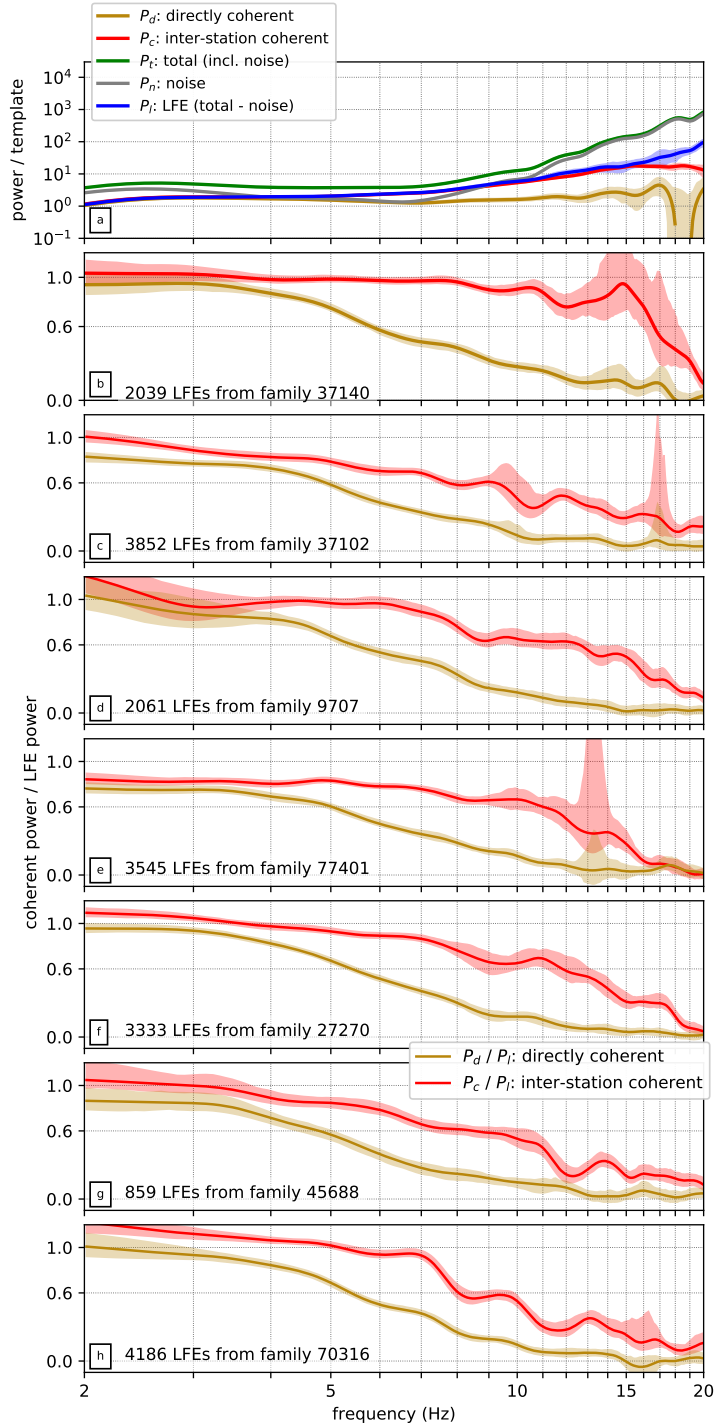


Figure 4: (a) Coherent and incoherent powers, as in Figure 3d, but averaged over 2000 LFEs from family 37140. Color indicates the power of interest. In all panels, the line indicates the value obtained with all allowable LFEs, and the shaded region delimits 95% confidence intervals obtained by bootstrapping the included events. (b-h) Ratios of the direct and inter-station coherence: P_c/P_l (yellow) and P_d/P_l (red). Each panel is computed for a different LFE family, as indicated by the text in the bottom left.

331 5 Hz. The decrease in direct coherence could imply (1) that the LFE source time functions are more
332 different at higher frequencies, (2) that the LFEs are too poorly aligned to show direct coherence at
333 high frequencies, or (3) that the stacking has modified the source time functions being compared.
334 We have tried improving the alignment by using higher-frequency signals in the alignment cross-
335 correlation, outside the 2 to 5-Hz range. We find that using higher frequencies in the alignment
336 does result in large P_d/P_l out to higher frequencies, but we choose not to use that alignment here
337 because some of the increase in P_d/P_l could come from the alignment of high-frequency noise.

338 Family 37140's inter-station coherent power P_c/P_l is insensitive to the alignment, and it re-
339 mains coherent over a wider frequency range. P_c/P_l is above or around 0.8 at frequencies up
340 to 15 Hz and falls below 0.6 only at 16.5 Hz. The persistence of high P_c/P_l out to frequencies
341 >15 Hz suggests that the ASTFs vary little among stations at >0.07 -second periods. We will use
342 synthetic rupture calculations to interpret this high-frequency coherence in terms of LFE rupture
343 area in section 7.

344 The other six LFE families show slightly lower coherence, as seen in Figure 4c-h and in Fig-
345 ures S8 - S14. Family 37102, the other family with an estimated duration (*Thomas et al.*, 2016),
346 displays gradually decaying P_d/P_l and P_c/P_l (Figures 4b and S9). Its P_d/P_l falls below 0.6 at
347 4 Hz, and its P_c/P_l stays above or hovers near 0.6 until 9 Hz. For the remaining families, the direct
348 coherence P_d/P_l remains above 0.6 out to 4 to 5 Hz. The inter-station coherence P_c/P_l remains
349 above 0.6 out to 8 to 13 Hz: to 8, 9, 11, 12, and 13 Hz.

350 These high-coherence frequency limits are likely lower bounds on the true high-coherence
351 frequencies. Our coherence estimates could be affected by a range of factors, including LFE
352 clustering, data selection, LFE origin time alignment, and template accuracy. We describe the
353 uncertainties in Appendix A1 and note that only the LFE origin time alignment is likely to give
354 artificially high coherence, and it affects only P_d/P_l , not P_c/P_l . The remaining factors would
355 result in our underestimating the true P_d/P_l and P_c/P_l . In section 7, we will therefore interpret
356 our coherence estimates as lower bounds on the true coherence when we consider the estimates'
357 implications for LFE rupture areas and location distributions.

358 **6 Frequencies With Coherent Power: Synthetics**

359 To consider the coherence's implications for LFE rupture areas, we need to know how P_d/P_l and
360 P_c/P_l depend on LFE rupture properties. So we generate and analyze groups of synthetic LFEs
361 with various diameters D , rupture velocities V_r , and rise times t_r . We create synthetic ruptures for
362 three types of LFEs (section 6.1), analyze their waveforms (section 6.2), and examine the coherent
363 frequencies as a function of the LFE properties (section 6.3).

364 **6.1 Synthetic LFEs Models**

365 We create and analyze groups of 100 LFEs. The individual events are assigned diameters D ,
366 rupture velocities V_r , and rise times t_r that cluster around specified mean values. The diameters,
367 rupture velocities, and rise times are chosen from lognormal distributions with factor of 1.3, 1.1,
368 and 1.3 standard deviations, respectively. Moments are chosen from lognormal distributions with
369 factor of 1.5 standard deviation and assigned with no consideration of the radii.

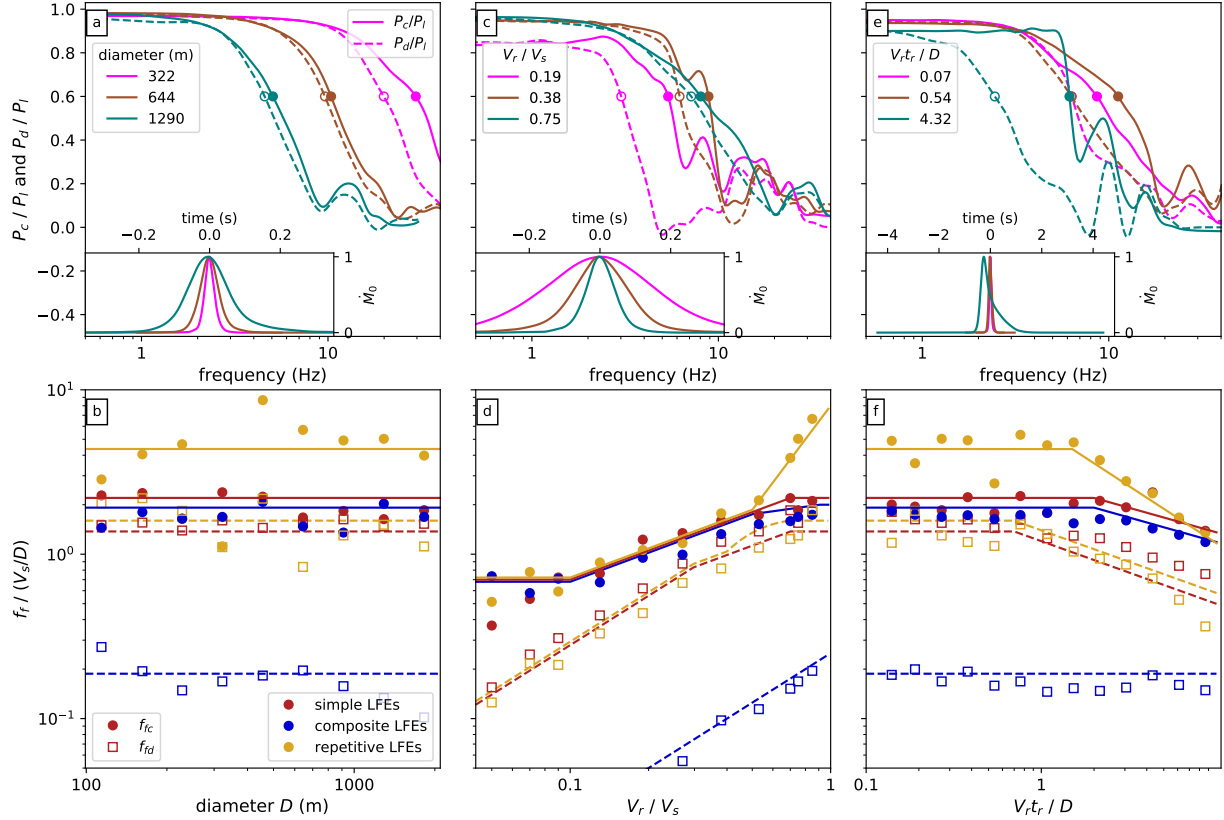


Figure 5: (a, c, e) Coherent power fractions P_c/P_l (solid lines) and P_d/P_l (dashed lines) as a function of frequency for various groups of synthetic LFEs. Circles mark the coherence falloff frequencies: when P_c/P_l or P_d/P_l falls below 0.6. Inset panels show the moment rate functions averaged over LFEs in each group. Color indicates diameter (panel a), rupture velocity (panel c), and rise time (panel e). (b, d, f) Normalized coherence falloff frequencies $f_{fc}/(V_s/D)$ (filled circles) and $f_{fd}/(V_s/D)$ (open squares) as a function of the LFE properties. Color indicates the type of LFE rupture. Solid and dashed lines indicate visually estimated approximations of the numerically identified f_{fc} and f_{fd} to be used in our interpretations. In panels a, b, c, and d, $t_r = 0.27D/V_r$. In panels a, b, e, and f, $V_r = 0.75V_s$. In panels c and e, $D = 456$ m. In panels d and f, the values plotted are medians taken from synthetics with 7 different diameters.

370 In the simplest version of our LFEs, each event is assigned a random heterogeneous slip dis-
 371 tribution within a roughly circular area, as detailed in section S4 and motivated by inferences of
 372 fractal earthquake slip distributions (Frankel, 1991; Herrero and Bernard, 1994; Mai and Beroza,
 373 2002). Rupture initiates at a random location within $0.4D$ of the center and spreads radially at rate
 374 V_r . Once a location starts slipping, slip accumulates following a regularized Yoffe function with
 375 duration t_r (Tinti et al., 2005).

376 We also construct groups of LFEs with more repetitive rupture patterns, as it is possible that
 377 LFEs within a given family recur not just on the same patch, but with similar rupture patterns within
 378 that patch (e.g., Ariyoshi et al., 2009; Ando et al., 2010; Sweet et al., 2014; Chestler and Creager,
 379 2017b). In our repetitive LFEs, slip is the sum of two heterogeneous distributions: one that varies
 380 randomly from event to event and one that is the same from event to event. The distributions

381 are scaled so that the repetitive component contributes twice as much moment, and slip always
382 nucleates within $0.1D$ of the LFE center points.

383 Finally, we construct groups of composite LFEs, as it is possible that individual LFEs comprise
384 a series of small ruptures of the complex fault zone at depth (Fagereng *et al.*, 2014; Hayman and
385 Lavier, 2014; Chestler and Creager, 2017b; Rubin and Bostock, 2017). Each of our relatively
386 crude composite LFEs contains five simple ruptures whose rupture velocities, diameters, and slip
387 distributed are chosen from the lognormal and heterogeneous distributions described above. The
388 five sub-ruptures begin at random times within a $2.5D/V_r$ interval.

389 6.2 Computing and Analyzing LFE Waveforms

390 Having defined the location and timing of slip in the LFEs, we compute ASTFs for nearby stations.
391 We assume that the synthetic LFEs are in the location of family 37140 and calculate ASTFs for the
392 12 stations used in its analysis, as shown in Figures 2 and S1. To calculate ASTFs, we integrate
393 the slip rate over the slipping area at each time step, but shift the signals' arrival times to account
394 for the travel time from each point in the source region to the observing stations, as in equation (2).
395 To calculate seismograms, we convolve these ASTFs with fake Green's functions, which are taken
396 to be white noise tapered by an exponential with a 3-s decay constant. We obtain similar results,
397 with maximum coherent frequencies 10 to 20% smaller, if we take instead take local earthquake
398 records as the Green's functions to create synthetic seismograms (Figure S26).

399 We may now process the synthetic seismograms. As with the real data, we create templates for
400 each LFE group, normalizing the synthetic seismograms by their maximum values and stacking.
401 We iterate the stacks three times. Each time, we cross-correlate the template seismograms with
402 the individual LFEs' waveforms. We identify a station-averaged time shift for each LFE, realign
403 according to those shifts, and stack.

404 Next, we use the templates to compute the cross-spectrum \hat{x}_{jk} for each synthetic LFE record
405 (equation (4)). As with the real data, we compute the cross-spectra from the tapered cross-
406 correlations, but we adjust the taper duration to ensure that it is always significantly longer than
407 the LFEs' durations. Finally, we compute the LFEs' template-normalized powers P_c , P_d , and P_l
408 (equations (5), (7), and (9)). Figure 5a, c, and e shows the coherent power fractions P_d/P_l and
409 P_c/P_l obtained for simple LFEs with various diameters, rupture velocities, and rise times.

410 6.3 Coherence Falloff Frequencies as a Function of D , V_r , and t_r

411 6.3.1 Coherence Falloff with Diameter

412 As anticipated in section 2, both P_d/P_l and P_c/P_l decrease at lower frequencies (longer periods)
413 when the LFE diameters are larger (panel a). P_d/P_l falls off earlier when diameters are larger
414 because larger diameters imply longer ruptures, which allow for complexity and inter-LFE vari-
415 ability at lower frequencies. P_c/P_l falls off earlier because larger diameters imply larger shifts
416 in the source-station travel time within the rupture area, and thus allow for inter-station ASTF
417 variability at lower frequencies. To examine the coherence falloff systematically, we identify the
418 frequencies at which P_d/P_l and P_c/P_l first fall below 0.6. These falloff frequencies f_{fd} and f_{fc} are
419 normalized by V_s/D and plotted as a function of LFE diameter D in Figure 5b. In the simple LFE
420 simulations in Figure 5b, which have $V_r/V_s = 0.75$ and $t_r = 0.27R/V_r$, f_{fd} is roughly $1.4V_s/D$

421 (open red squares and dashed red line), and f_{fc} is roughly $2.2V_s/D$ (filled red circles and solid red
422 line).

423

424 **6.3.2 Coherence Falloff with Rupture Velocity**

425 The direct coherence falloff frequency f_{fd} decreases relative to V_s/D if LFE rupture velocities
426 are reduced, as shown Figure 5c and d. Note that when we plot $f_{fd}/(V_s/D)$ and $f_{fc}/(V_s/D)$ in
427 Figure 5d and f, we take the median of estimates computed for 7 groups of LFEs, with differ-
428 ent diameters, in order to reduce the scatter. The decrease of $f_{fd}/(V_s/D)$ with decreasing rupture
429 velocities arises because lower rupture velocities allow for longer ruptures and therefore more com-
430 plexity and inter-event variability at lower frequencies. The LFEs' heterogeneous slip distributions
431 give rise to source time functions that differ among events at all periods shorter than the rupture
432 duration, which scales as D/V_r in simulations of simple LFEs. The direct coherence falloff fre-
433 quency f_{fd} thus scales inversely with the durations of these ruptures, with value around $2.8V_r/D$
434 when $V_r < 0.4V_s$, though it decreases relative to V_r/D for rupture velocities larger than $0.8V_s$ (red
435 dashed line in Figure 5d).

436 The inter-station coherence falloff frequency f_{fc} depends more weakly on rupture velocity V_r .
437 f_{fc} increases from 0.7 to $2.2V_s/D$ as V_r increases from 0.05 to $1V_s$ (filled red circles and solid
438 red line in Figure 5d). P_c/P_l depends only weakly on V_r because P_c/P_l measures how much
439 the ASTFs vary among stations, not among events. The inter-station ASTF variability depends
440 primarily on the S-wave travel time across the source region, which scales with D/V_s , not D/V_r .
441 The V_r dependence that does exist likely results from the simpler ASTF pulses associated with
442 higher rupture velocities. As V_r approaches V_s , the ASTFs tend toward single pulses, and inter-
443 station complexity is harder to distinguish.

444 **6.3.3 Coherence Falloff With Rise Time**

445 Both f_{fd} and f_{fc} vary minimally in response to modest changes in the rise time t_r of slip at each
446 point in the rupture, especially when t_r is less than D/V_r (Figure 5c and f). In our implementation,
447 we have assumed a spatially uniform rise time for each LFE. As a result, changing the rise time is
448 roughly equivalent to convolving all of an LFE's ASTFs by a single function, and such a convo-
449 lution has little effect on the inter-ASTF coherence. We do allow roughly 10% variability in rise
450 time and rupture velocity among the LFEs in each group. These rise time differences, coupled with
451 the increased complexity visible in longer-duration ruptures, are likely responsible for the reduced
452 coherence falloff frequencies that become apparent once t_r exceeds 1 to $2D/V_r$ (red symbols and
453 lines in Figure 5d).

454 **6.3.4 LFE Durations**

455 Increasing the rise time does increase LFE duration. To estimate an average duration for each group
456 of 100 synthetic LFEs, we first extract the source time functions for the individual LFEs. We shift
457 these source time functions using the time shifts estimated via cross-correlation when constructing
458 the waveform template. Then we sum the source time functions to obtain an average source time
459 function, or moment rate function. Finally, to obtain a single number that we can compare across

460 simulations with a range of parameters, we define a 70% LFE duration: the length of the time
461 interval that contains the central 70% of the moment for the average moment rate function.

462 We find that in our simple LFEs, these 70% durations are between 0.29 and $0.31D/V_r$ when
463 the rise time t_r is $0.27D/V_r$. The durations increase as t_r is increased, and tend toward $0.28t_r$ once
464 t_r gets significantly longer than D/V_r .

465 LFE durations are shorter in synthetic ruptures that nucleate near the rupture centers. For our
466 repetitive LFEs, which we assume nucleate within $0.1D$ of their center points, durations are 0.25
467 to $0.28D/V_r$ when t_r is $0.27D/V_r$. LFE durations are longer in synthetic ruptures that nucleate
468 near the rupture edges. The durations are between 0.35 and $0.37D/V_r$ when nucleation locations
469 are within $0.1D$ of the rupture edge. The durations of composite LFE ruptures are determined by
470 the number and timing of subevents. The presented LFEs, containing 5 subevents, have durations
471 between 3 and $3.3D/V_r$.

472 6.3.5 Composite LFEs

473 The composite LFEs, with their long, complex ruptures, have lower direct coherence P_d/P_l than
474 the simple LFEs. The direct coherence falloff frequency f_{fd} is around $0.25V_r/D$ for all simulated
475 events (open blue squares and dashed lines in Figure 5b, d, and f). On the other hand, the com-
476 posite and simple LFEs have similar inter-station coherence P_c/P_l and similar inter-station falloff
477 frequencies f_{fc} (filled blue circles and solid blue line). As for the simple ruptures, the composite
478 LFEs' P_c/P_l and f_{fc} depend primarily on D/V_s : on how much the source-station travel time can
479 shift peaks in the source time functions.

480 6.3.6 Repetitive LFEs

481 Repetitive LFEs can have significantly higher coherence and falloff frequencies than simple or
482 composite events, at least when the rupture velocity is larger than about $0.5V_s$. As described in
483 section 6.1, the repetitive LFEs simulated in each group have similar slip distributions, and they
484 all nucleate near the rupture center, so they have similar ASTFs and similar waveforms. This
485 similarity explains the increase in P_d/P_l , but the increase in P_c/P_l is surprising at first glance,
486 as P_c/P_l measures similarity across stations, not across events. The high P_c/P_l arises because
487 the cross-spectra calculation that goes into P_c (equation (4)) is designed to remove complexity
488 associated with the path effects, and it identifies as “path effect” any component of the source-
489 path convolution (equation (3)) that is common to all events. If the ASTFs are the same for all
490 events, the P_c calculation cannot distinguish inter-station ASTF variations from station-dependent
491 Green's functions, so ASTF variations are attributed to path effects, and P_c/P_l is high when LFEs
492 are highly repetitive. The falloff frequencies f_{fc} can increase by as much as factor of 6 when
493 $V_r > 0.8V_s$.

494 We note, however, that this factor of 6 increase in f_{fc} is just one plausible value. Here we have
495 assumed that two-thirds of the LFE moment came from a repetitive component of the rupture, but
496 higher or lower coherence could be achieved by assuming that more or less of the moment came
497 from the repetitive component. We also note that the high coherence arises only when the rupture
498 nucleation location is consistent from event to event. The falloff frequencies f_{fc} remain low if only
499 75% of the repetitive LFEs nucleate at the SE rupture edge and the other 25% nucleate on the NW
500 edge (Figure S24).

6.3.7 Coherence Variation With Station Distribution

In all of the synthetic ruptures described above, we use the station distribution and LFE location appropriate for family 37140, because using this station distribution allows us to directly compare the synthetics with the data. Note that most of the stations are located southeast of the LFEs, so the seismic waves' takeoff angles and thus the LFEs' ASTFs are more similar among these stations than they would be among stations were located at a wider range of azimuths. We find that P_d/P_l and P_c/P_l decreases at frequencies that are 10 to 20% lower when we assign the recording stations to random azimuths (Figures S21 and S22). Simply reducing the number of stations creates no such coherence reduction, however. The coherent frequencies change minimally if we pick subsets of the stations for each computation, to mimic the varying data availability and noise level (Figure S20).

7 Interpretation of LFE Coherence

We may now use our synthetic results to interpret the coherence obtained for the Parkfield LFE families, which show direct coherence $P_d/P_l > 0.6$ out to 4 to 5 Hz and inter-station coherence $P_c/P_l > 0.6$ out to 8 to 16.5 Hz.

7.1 LFE Location Distribution

First, we note that the observed high-frequency coherence implies that LFEs within each family are strongly clustered in space. If LFEs were distributed over a wide range of locations, travel times from the LFE centroids to the recording stations would vary widely from event to event. But in our analysis, we allow only the origin time to be realigned from event to event. Any inter-station time shifts produced by varying LFE locations should show up in our results as a decrease in coherence.

To determine the maximum location variation allowed by the observations, we recompute coherence values after artificially shifting the LFE locations by various amounts. We pick location shifts for each LFE in family 37140, drawing from bivariate normal distributions with 100-m to 1-km standard deviations along strike and depth. We use the IASP91 velocity model and TauP to compute the arrival time change for the stations observing each LFE (Kennett and Engdahl, 1991; Crotwell *et al.*, 1999). We subtract the median arrival time change from these values, shift the seismograms by the station-dependent remainders, and compute the coherent power fractions. The family-averaged results are shown in Figures 6 and S15-S17. We find that the inter-station coherent fraction P_c/P_l obtained at 11 Hz is reduced by 40% even for location shifts with just 250-m standard deviation (Figure 6). The > 0.6 11-Hz coherence values obtained for the median family thus imply that LFEs in each family are strongly clustered, with standard deviation in their locations typically smaller than 250 m.

The distribution of LFE locations within a family, when coupled with noise, is one way to explain all of the incoherence observed at higher frequencies in the data. It is possible that each individual LFE is approximately a point source—that each LFE ruptures a tiny patch within a sub-1-km asperity (Chestler and Creager, 2017a).

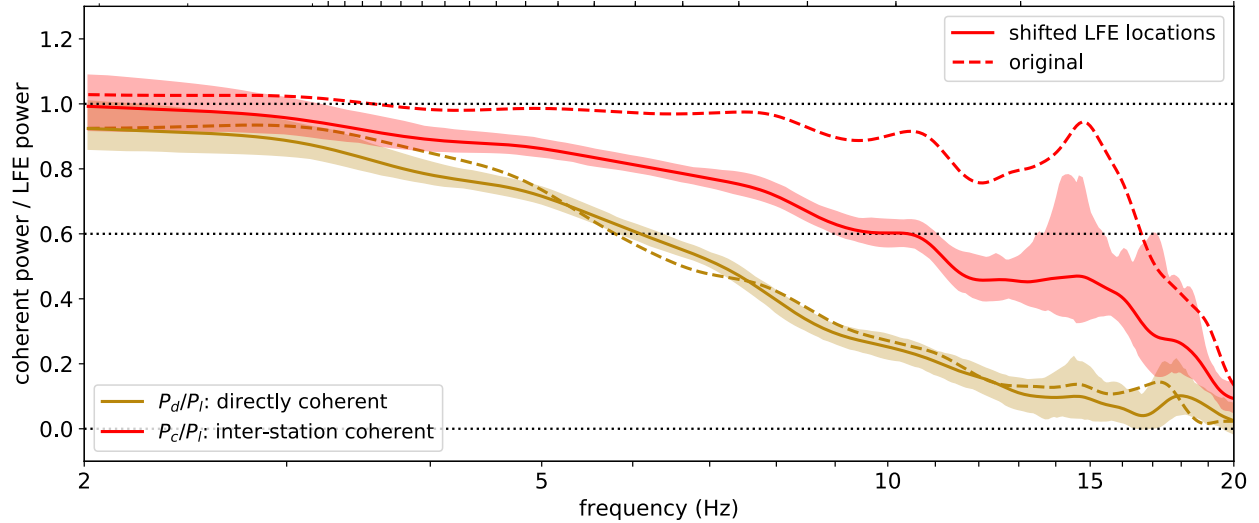


Figure 6: Solid lines and shading: coherent power fractions for family 37140, as in Figure 4b, but computed after shifting the LFE locations by random amounts with 250-m standard deviations along strike and along depth. Dashed lines: original P_d/P_l and P_c/P_l , without location shifts, reproduced from Figure 4b.

7.2 Matching f_{fc} , f_{fd} , and Duration With Simple Ruptures: Results

However, it is also possible that the finite rupture areas of individual LFEs contribute to the decrease in coherence at high frequencies. To determine the maximum rupture areas and rupture velocities allowed by the data, we compare the observed coherence falloff frequencies and durations with those obtained from synthetics of simple, non-repetitive ruptures.

First, we note that the inter-station coherence P_c/P_l remains higher than 0.6 out to 8 to 16.5 Hz for the various families. The median P_c/P_l falloff frequency f_{fc} is 11 Hz, and families 37102 and 37140 have f_{fc} of 9 and 16.5 Hz, respectively. We will discuss these families in more detail because *Thomas et al.* (2016) estimated their LFEs' durations, and so we will be able to estimate their rupture velocities. In the synthetics, f_{fc} is 0.7 to $2.2V_s/D$ for rupture velocities V_r between 0.05 and $1V_s$ (red solid line in Figure 5d). If the shear wave velocity V_s is around 4 km/s in the LFE area (*Lin et al.*, 2010), family 37102's 9-Hz f_{fc} implies an average diameter smaller than 300 to 1000 m, with smaller allowable diameters for slower rupture velocities. In Figure 7a, this range of allowable diameters is marked with blue diagonal hatching. The blue shading marks the diameters allowed for family 37140. Its >16-Hz f_{fc} implies diameters smaller than 180 to 550 m.

The orange diagonal hatching in Figure 7a illustrates a further, albeit weaker, constraint on the LFEs' diameters and rupture velocities: those obtained from the direct coherence P_d/P_l . P_d/P_l is higher than 0.6 out to 4 to 5 Hz for all seven LFE families, though it could be biased high or low by uncertainties in the LFE origin time alignment (see Appendix A1). In the synthetics, the P_d/P_l falloff frequency f_{fd} scales roughly with 1 divided by the rupture duration. f_{fd} ranges from 1.4 to $2.8V_r/D$, or from 0.15 to $1.4V_s/D$ (blue dashed line in Figure 5d). Coupling the synthetics with a 5-Hz observed f_{fd} constrains the LFE diameters to be less than 1100 m.

More important constraints on the LFE properties come from the LFE durations estimated by *Thomas et al.* (2016). *Thomas et al.* (2016) compared LFE stacks with nearby earthquakes'

562 waveforms and obtained best-fitting durations of 0.19 and 0.22s for LFEs in families 37140 and
 563 37102, respectively. To get a sense of the duration uncertainty, we note that *Thomas et al. (2016)*'s
 564 best fits come from averaging over comparisons with 12 or 17 different local earthquakes, but they
 565 also present the durations obtained by the individual earthquake comparisons. Only one earthquake
 566 comparison gives a family 37140 duration smaller than 0.15 or larger than 0.22, and only one
 567 comparison gives a family 37102 duration smaller than 0.15 or larger than 0.3, so we use these
 568 values as uncertainty bounds.

569 To compare the durations to our synthetics, we note that 70% of the moment in the stacked
 570 synthetic LFEs accumulates within 0.29 to $0.31V_r/D$. *Thomas et al. (2016)* modeled the LFE
 571 waveforms with a source time function shaped like a Hann window, which accumulates 70% of
 572 its moment within 40% of the total window length, so the 70% durations for families 37140 and
 573 37102 are 0.060 to 0.087 and 0.060 to 0.12 s, respectively. We multiply these 70% durations by 1.4
 574 to $2.8V_r$ to estimate LFE diameters and plot the results with red shading in Figure 7a. The lower
 575 and upper thick red lines mark the diameters expected for the best-fitting durations for families
 576 37140 and 37102, respectively.

577 The diameters implied by the observed durations match those implied by family 37102's >9 Hz
 578 f_{fc} for a wide range of rupture velocities. The two sets of constraints overlap at least partially for
 579 all plotted V_r/V_s , and the inter-station coherence constraint matches the median duration when
 580 $V_r < V_s$. According to these results, LFEs in family 37102 could be slow ruptures, with 200-
 581 m diameters and $V_r = 0.2V_s$. Or they could be relatively "normal" earthquakes, with 800-m
 582 diameters and $V_r = 0.8V_s$. Note that changing the assumed shear wave velocity V_s would change
 583 the estimated diameters in Figure 7, but not the V_r/V_s intersection ranges, as all of the plotted
 584 diameter constraints scale with $1/V_s$.

585 Given the uncertainties in the data, the constraints on LFEs in family 37140 could also be
 586 matched with a range of rupture speeds. This family's $f_{fc} > 16$ Hz constraint (blue shading
 587 in Figure 7a) starts to intersect the edge of the duration constraints when $V_r < 0.7V_s$. Note,
 588 however, that the plotted 16-Hz constraint is already the 95% lower bound on f_{fc} , obtained from
 589 bootstrapping. The best-fitting f_{fc} is 16.5 Hz. Lower rupture speeds would match the data better.
 590 For instance, to match family 37140's best-fitting duration (lower red line) and the constraint that
 591 $f_{fc} \gtrsim 16$ Hz (blue shading), the LFE rupture speeds should be less than $0.4V_s$.

592 **7.3 Matching f_{fc} , f_{fd} , and Duration With Simple Ruptures: Uncertainties**

593 There are several uncertainties in the data and models that are not represented with the bootstrap-
 594 based uncertainty bounds. We consider how these would influence the rupture velocity estimates.
 595 For instance, one might imagine that all ruptures begin at the asperity edge and rupture unilaterally.
 596 In synthetics, groups of synthetic ruptures starting within $0.1D$ of the LFE edge have durations of
 597 0.35 to $0.37D/V_r$, longer than the 0.29 to $0.31D/V_r$ values estimated for events starting within
 598 $0.4D$ of the center. Interpreting *Thomas et al. (2016)*'s durations via unilateral rupture would
 599 cause our duration-estimated diameters to decrease by about 20% moving the red lines in Figure 7a
 600 down. However, synthetic ruptures starting from the edge also give f_{fc} values about 20% smaller
 601 than those starting closer to the center (Figure S19). Changing both constraints thus moves both the
 602 red and blue lines down in Figure 7a, and leaves the range of allowable rupture velocities almost
 603 unchanged.

604 Other minor modifications to the rupture parameters appear to affect the f_{fc} constraints min-
605 imally. For instance, we observe little change in f_{fc} if we add a smooth tapered component to
606 the heterogeneous slip distributions (Figure S23) or if we limit the range of diameters within each
607 group to a factor of 1.1 standard deviation (Figure S25). However, we have not explored the
608 entire range of rupture parameters. Perhaps we would obtain higher coherence if we made the
609 slip distribution and temporal evolution smoother or slightly more repetitive, more similar to the
610 repeater-like LFEs discussed in sections 6.1 and 7.4.

611 Another scenario that seems unlikely but possible is that the 16.5-Hz f_{fc} obtained for family
612 37140 reflects random variability in the data or noise. This f_{fc} is significantly larger than the
613 median f_{fc} for the seven families, which is just 11-Hz, and the synthetics in Figure 5b do show
614 tens of percent variability in f_{fc} among LFE groups, simply as a result of random variations in
615 the slip distributions. However, those synthetics use only 100 LFEs. Using several thousand
616 should reduce the uncertainty. Further, bootstrapping events within each synthetic group gives a
617 reasonable estimate of the variability among the groups. Bootstrapping the data in family 37140
618 gives 95% probability that $f_{fc} > 16$ Hz.

619 The other uncertainties in the data, along with potential variation in LFE location, would imply
620 that the estimated 16.5-Hz f_{fc} is a lower bound on the true value, as discussed in section 5 and
621 appendix A1. Accounting for noise or variable LFE locations would push the allowable diameters
622 and the blue shading in Figure 7a down to lower values, making it harder to match the data with
623 high rupture speeds. Given the uncertainties, we cannot exclude the possibility that these LFEs are
624 simple ruptures with “typical” earthquake rupture speeds around $0.7V_s$. But we consider it more
625 likely that the rupture velocities are lower than $0.7V_s$ (blue and red shading in Figure 7a). The data
626 are best matched by simple LFEs when rupture velocities are less than $0.4V_s$ (blue shading and red
627 line).

628 7.4 Matching the Data With Modified LFE Ruptures

629 It is also possible to match the data if we modify the LFE dynamics significantly: if LFEs are
630 composite ruptures, ruptures with long rise times, or repetitive ruptures, as described in section 6.1.
631 Figure 7b-d illustrates the constraints obtained for some plausible rupture parameters.

632 Figure 7b illustrates the constraints on diameters and rupture velocity if LFEs are composed
633 of 5 sub-ruptures distributed over an interval with duration $2.5D/V_r$. Here the inter-station coher-
634 ence constraints (blue) are essentially unchanged, but the direct coherence and duration constraints
635 imply smaller diameters.

636 Figure 7c illustrates the constraints if LFEs have rise times equal to $5D/V_r$. In these LFEs,
637 rupture would progress to the asperity edge, and then the whole patch would continue slipping
638 together.

639 Finally, Figure 7d illustrates the constraints on D and V_r/V_s if LFEs are repetitive ruptures,
640 which persistently nucleate in the same region, and which have two-thirds of their moment asso-
641 ciated with a slip distribution that is consistent from event to event. With these repetitive ruptures,
642 the 16-Hz f_{fc} of family 37140 can be matched even if the rupture diameters are larger.

643 A wide range of parameters could also match the data if LFE durations are actually reflections
644 of local attenuation, not the LFE source dynamics (Gomberg *et al.*, 2012; Bostock *et al.*, 2017). In
645 this case, the diameters estimated from the durations (red lines) are upper bounds, and the data can

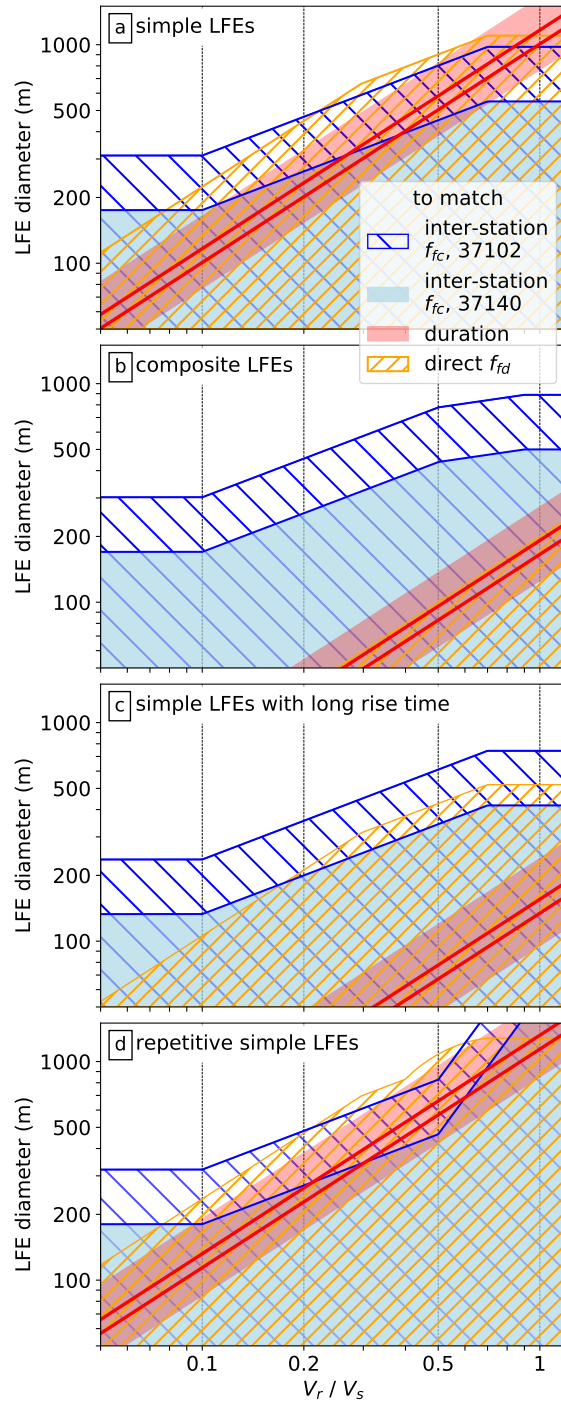


Figure 7: Hatching and shading: sets of diameters (y-axis) and rupture velocities (x-axis) that match each of the observations. Blue hatching and shading match f_{fc} for families 37102 and 37140, respectively. Yellow hatching matches the median f_{fd} for all families. Red shading matches the range of durations of *Thomas et al.* (2016), and the red lines match their best-fitting durations. The four panels are for four approaches to constructing the LFEs, as indicated by the text in the upper left.

646 be matched by any combination of rupture velocity and diameter that plots below those bounds
647 and within the f_{fc} (blue) and f_{fd} (yellow) constraints.

648 **8 Discussion**

649 **8.1 Implications for Tremor Asperities**

650 Regardless of the individual LFE rupture dynamics, our observations of high-frequency coherence
651 suggest that LFEs are clustered in patches less than 1 km across. As noted in the introduction,
652 such clustering has also been inferred from careful analysis of LFE families in Cascadia (*Sweet*
653 *et al.*, 2014; *Chestler and Creager*, 2017a) and may be suggested by highly periodic LFE rup-
654 tures in Parkfield (*Shelly*, 2010b). The clustering may suggest a role for material heterogeneity
655 in controlling the occurrence of tremor. It is consistent with proposals that tremor’s LFEs rupture
656 a collection of unstable asperities embedded in a larger, more stable region (*Ando et al.*, 2010;
657 *Nakata et al.*, 2011; *Ando et al.*, 2012; *Ariyoshi et al.*, 2012; *Veedu and Barbot*, 2016; *Luo and*
658 *Ampuero*, 2017). Larger asperities may also exist, as patches of tremor are observed on scales
659 of a few to tens of km. The larger tremor patches could represent groups of tremor asperities or
660 regions more prone to distributed rapid slip (*Shelly*, 2010b; *Ghosh et al.*, 2012; *Armbruster et al.*,
661 2014; *Yabe and Ide*, 2014; *Savard and Bostock*, 2015; *Annoura et al.*, 2016; *Kano et al.*, 2018).
662 Alternatively, the large and small tremor patches could represent persistent slip patterns that have
663 arisen on a simple, homogeneous fault. Such patterns are sometimes seen in models that lack het-
664 erogeneity in material properties (*Horowitz and Ruina*, 1989; *Langer et al.*, 1996; *Shaw and Rice*,
665 2000), though it remains to be assessed whether these models can produce clusters of tremor that
666 persist over many slow slip cycles, as we observe in Parkfield.

667 The family-based clustering implied by our coherence estimates and by others’ LFE relocations
668 (*Sweet et al.*, 2014; *Chestler and Creager*, 2017a) suggests that cross-correlation based LFE fam-
669 ilies are more than an observational convenience (*Shelly et al.*, 2007; *Brown et al.*, 2008; *Bostock*
670 *et al.*, 2012; *Frank et al.*, 2013; *Kato*, 2017; *Shelly*, 2017). The analyzed families show sub-km
671 LFE clustering even though some families are separated from identified neighboring families by a
672 few to 5 km. The LFEs’ tendency to occur on these asperities lends further confidence to studies
673 that have interpreted LFE repeat rates as indicators of the slip rate in a creeping area surrounding
674 the more unstable LFE patches (*Rubin and Armbruster*, 2013; *Royer et al.*, 2015; *Lengliné et al.*,
675 2017; *Thomas et al.*, 2018).

676 **8.2 Implications for Tremor Physics**

677 Given our observations and synthetics of LFE coherence as a function of rupture diameter, there
678 are still several ways to explain the long, 0.2-s durations of Parkfield LFEs. First, it is possible that
679 families 37102 and 37140’s LFEs are normal earthquakes with near-shear-wave rupture speeds. A
680 $0.7V_s$ rupture speed is at the edge of the constraints for family 37140, but it can match the con-
681 straints on family 37102 well, and it may be worth noting that family 37140 shows exceptionally
682 high coherence while Family 37102 has coherent power profiles that are more similar to the pro-
683 files of the other five families, for which we cannot estimate rupture velocities because we do not
684 know their durations.

685 Further, $0.7V_s$ rupture velocities could match the data better if the LFEs are somewhat repeti-
686 tive, with nucleation locations and slip distributions that persist from event to event. And a wide
687 range of high rupture speeds could match the data if the 0.2-s durations we use are overestimates
688 of the true durations, despite *Thomas et al. (2016)*'s careful empirical Green's function analysis.
689 The durations could be overestimated if a highly attenuating region is localized around the LFE
690 patches, so that attenuation removes the high-frequency components of the LFE seismograms but
691 has little effect on the seismograms of the reference earthquakes, which are located a few km away.

692 If LFEs do have durations of 0.2 s and rupture speeds up to $0.7V_s$, they could have diameters
693 up to 800 m. Uniform stress drop M_W 1 to 2 earthquakes with 800-m diameters would have stress
694 drops of 0.3 to 9 kPa and average slips of 0.002 to 0.06 mm (*Eshelby, 1957; Shearer, 2009*). These
695 moment and slip estimates are imprecise, and difficult to estimate because LFE locations are offset
696 from local earthquakes, but we note that if the larger slip estimates are representative, almost all of
697 the slip on the LFE patch could be seismic. Even 800-m-wide LFEs could accommodate most of
698 the long-term slip on the LFE patch, which *Thomas et al. (2016)* estimated to be around 0.05 mm
699 per event.

700 But while LFEs from both families can be matched by rupture velocities up to $0.7V_s$, the data
701 from family 37140 are better matched by LFEs with slower rupture speeds ($< 0.4V_s$), long rise
702 times, or a composite of subevents. Any of these scenarios would have interesting implications
703 for the physics of LFE ruptures. For instance, rupture speeds around $0.4V_s$, which can match the
704 data for both families, would suggest that the LFEs' radiation efficiency is around 0.5: that about
705 half of the energy in LFEs is released via seismic wave generation, with the rest expended as
706 fracture energy (e.g., *Kostrov, 1966; Eshelby, 1969; Fossum and Freund, 1975; Venkataraman and*
707 *Kanamori, 2004; Kanamori and Rivera, 2006*). Such low but significant radiation efficiency *could*
708 mean that LFEs are exceptionally weak but otherwise normal earthquakes; LFEs may be driven
709 by unstable frictional sliding, with slip rates limited by seismic wave radiation. Although $0.4V_s$
710 is lower than typical earthquake rupture speeds (*McGuire, 2004; Seekins and Boatwright, 2010;*
711 *Folesky et al., 2016; Ye et al., 2016; Melgar and Hayes, 2017; Chouinet et al., 2018*), such speeds
712 are sometimes observed in earthquakes, especially in shallow tsunami earthquakes (e.g., *Ide et al.,*
713 *1993; Ihmlé et al., 1998; Venkataraman and Kanamori, 2004; Bilek and Engdahl, 2007; Polet and*
714 *Kanamori, 2009; Cesca et al., 2011*).

715 It is thus possible that LFEs are simply earthquakes driven by a frictional weakening process
716 that is for some reason smaller in magnitude than the processes driving normal earthquakes. LFEs
717 might nucleate "earlier" than most earthquakes, at times when there is only a modest stress drop
718 available to drive rupture. Or LFEs could nucleate on small unstable patches but then move quickly
719 into regions that resist high slip speeds, perhaps because they are velocity-strengthening or allow
720 for large off-fault deformation. Such acceleration-resisting regions have been suggested to limit the
721 rupture velocities of tsunami earthquakes (e.g., *Bilek and Lay, 2002; Faulkner et al., 2011a; Ma,*
722 *2012*). Off-fault deformation seems an appealing process to invoke for tremor because complex
723 brittle and ductile deformation is observed at relevant depths (*Fusseis et al., 2006; Handy et al.,*
724 *2007; Collettini et al., 2011; Fagereng et al., 2014; Hayman and Lavier, 2014; Angiboust et al.,*
725 *2015; Behr et al., 2018; Webber et al., 2018*). It is even possible that each LFE is a collection
726 of small brittle failures, rupturing small faults or veins (*Fagereng et al., 2014; Ujiie et al., 2018*).
727 However, it remains unclear how or if that distributed ductile deformation would limit the rupture
728 speeds of LFEs. Off-fault ductile deformation is also thought to accumulate in large earthquakes,
729 which have near-shear-wave rupture speeds (*DeDontney et al., 2011; Dunham et al., 2011; Roten*

730 *et al.*, 2017).

731 Another possibility is that LFEs do rupture at near-shear-wave speeds, but that the shear wave
732 speed is significantly reduced in the LFE area because of lithological variations, fault zone damage,
733 or high pore pressures (Audet *et al.*, 2009; Song *et al.*, 2009; Kato *et al.*, 2010; Fagereng and Di-
734 ener, 2011; Stefano *et al.*, 2011; Huang *et al.*, 2014). Fault damage zones are frequently observed
735 at a range of depths (Shipton and Cowie, 2001; Rowe *et al.*, 2009; Faulkner *et al.*, 2011b; Rempe
736 *et al.*, 2013; Leclère *et al.*, 2015), and they sometimes show 30 to 50% reductions in wavespeed, at
737 least in shallow regions (Ben-Zion *et al.*, 2003; Cochran *et al.*, 2009; Lewis and Ben-Zion, 2010;
738 Yang *et al.*, 2014; Li *et al.*, 2016). It is difficult to fully assess a low-wavespeed region’s implica-
739 tions for our observations. The inter-station coherence we observe depends on the seismic waves’
740 source-station travel times, and those times depend on which source-station paths are traveled. But
741 in the simplest case, where LFE signals begin by traveling horizontally away from the fault, so
742 that they move outside the fault zone before continuing to the surface, the travel time variation
743 we probe with inter-station coherence would depend primarily on the higher wavespeed outside
744 the fault zone. The higher wavespeeds could allow for the high-frequency inter-station coherence
745 we observe even though the lower wave speed inside the fault zone limits the rupture velocity and
746 produces long-duration events.

747 On the other hand, it is possible that LFE rupture velocities are not limited by seismic wave
748 radiation at all, but by a different fault zone rheology. We note that the results from family 37140
749 are best fit by simple LFE ruptures with $V_r < 0.4V_s$, and because of noise in the data, all of our
750 coherence-constrained diameters and rupture speeds are upper bounds on the true values. So LFE
751 rupture speeds could be much smaller: $0.2V_s$, for example. Such slowly rupturing LFEs would
752 release more than 80% of their energy via fracture energy, making it unlikely that the energy dis-
753 sipated via seismic wave radiation could limit the slip speeds. The low rupture velocities inferred
754 for family 37140 could be telling us that LFE rupture dynamics are controlled by a different defor-
755 mation mechanism than normal earthquakes—perhaps by the same speed-limiting rheology that
756 controls slow slip events (e.g., Ide *et al.*, 2007; Shibazaki and Iio, 2003; Shibazaki and Shimamoto,
757 2007; Ide *et al.*, 2008; Aguiar *et al.*, 2009; Liu *et al.*, 2010; Segall *et al.*, 2010; Gao *et al.*, 2012;
758 Hawthorne and Rubin, 2013; Ide and Yabe, 2014; Hawthorne and Bartlow, 2018).

759 9 Conclusions

760 We have analyzed inter-station and inter-event coherence between LFEs in seven families near
761 Parkfield, CA. Our synthetic analysis shows that we can use inter-station ASTF variations to esti-
762 mate LFE location distributions or rupture areas. Our observations of LFE coherence imply that
763 LFEs in each family are clustered in a small region, with standard deviation in their locations
764 smaller than 250 m. Comparing the observed coherence with the coherence of synthetic LFE
765 ruptures implies that LFE diameters are smaller than 500 to 1100 m, depending on the family.
766 Coupling the diameter constraints with the LFE durations estimated by Thomas *et al.* (2016) for
767 families 37102 and 37140 has allowed us to assess plausible rupture velocities. We could match
768 the data for LFEs in family 37102 with a wide range of rupture models, including earthquake-like
769 ruptures with rupture velocities V_r of 0.7 to 0.9 times the shear wave speed V_s . $V_r = 0.7V_s$ can
770 also match the data for family 37140, but only on the edge of the constraints. The data are better
771 matched with lower rupture speeds $V_r < 0.4V_s$. Such low rupture speeds may indicate that LFEs

772 are governed by a slow slip rheology, not by unstable frictional sliding. Alternatively, the data
773 from both families of LFEs could be matched if LFEs rupture a fault zone with low shear wave
774 speed, or if LFEs are repetitive fast ruptures, composite ruptures, or ruptures with long rise times.
775 Our synthetics illustrate how the coherence and durations might differ among these rupture types,
776 and thus how we might probe the physics of LFEs with future observations.

777 Acknowledgments

778 We used seismic waveform data from the Berkeley Parkfield High Resolution Seismic Network
779 (HRSN), provided via the Northern California Earthquake Data Center and the Berkeley Seis-
780 mological Laboratory (doi: 10.7932/NCEDC), as well as seismic waveform data from the Plate
781 Boundary Observatory (PBO) borehole seismic network, operated by UNAVCO and funded by
782 NSF grant EAR-0732947. The PBO data was obtained via IRIS. The fault traces shown in Fig-
783 ure 2 were obtained from the USGS and California Geological Survey fault and fold database,
784 accessed from <http://earthquake.usgs.gov/hazards/qfaults> in 2016. We are grateful to David Shelly
785 for providing an earlier version of his Parkfield LFE catalog. We thank the editor and reviewers
786 for comments that improved the paper.

787 A1 Decoherence from Noise

788 Our coherence frequencies should probably be interpreted as lower bounds, as several sources of
789 noise could reduce the observed P_d/P_l and P_c/P_l from their true values. First, decreased P_d/P_l
790 and P_c/P_l could arise if a significant portion of the “noise” comes from LFEs that are nearby but
791 not in the family of interest. LFEs are clustered in space and time (e.g., *Shelly, 2010a; Bostock*
792 *et al., 2015*) so the noise from other LFEs may be higher during the LFE window than during the
793 noise window before it. We estimate the noise power P_n in a window that starts just 8 s before the
794 LFE S arrival to minimize the potential difference, but we cannot account for sub-8 s clustering.
795 Note that in principle our noise window could include some of the P arrival. However, we find
796 the P arrival is too late and too small to significantly affect the P_n estimates. Truncating the noise
797 waveforms before the P arrivals and reprocessing changes our results negligibly.

798 Decreased P_d/P_l and P_c/P_l could also result from noise in the template LFEs. The template
799 signals start to become poorly resolved at frequencies higher than 15 Hz, so it is difficult to calcu-
800 late robust powers at those frequencies. In addition, decreased P_d/P_l and P_c/P_l could arise if the
801 path effect varies spatially within the families’ source region, so that the template and individual
802 LFEs have different path effects.

803 Finally, decreased or increased P_d/P_l could result from uncertainty in the LFE origin time. To
804 accurately calculate direct coherence at high frequencies, we need well aligned waveforms, so we
805 re-compute LFE origin times using 0.01-s precision. The realignment affects P_c/P_l negligibly but
806 increases the frequencies with $P_d/P_l > 0.6$ by several Hz relative to results without recomputed
807 origin time. One might worry that the increase in coherence comes from aligning the template
808 with coherent noise rather than with LFE signal. However, we require at least 5 stations for the
809 power estimates for each LFE, and we allow only one origin time shift per LFE. Assuming noise
810 is random among stations, realigning with noise should increase P_d/P_l by less than 0.2.

811 The LFE detection approach of *Shelly* (2017) could also result in slightly increased coherence
812 if noise contributes a part of the identified coherent signals. Finally, slightly increased coherence
813 could result from our exclusion of signals with especially high noise. Note that the detected-
814 facilitated increases in coherence are most likely to occur at low frequencies, around a few Hz, as
815 these frequencies contribute most of the seismogram power involved in LFE selection and align-
816 ment.
817 There are no other obvious sources of artificially high coherence. Applying our processing to
818 noise intervals rather than LFEs gives P_c/P_l and P_d/P_l of 0.01 or less.

819 **References**

- 820 Aguiar, A. C., T. I. Melbourne, and C. W. Scrivner, Moment release rate of Cascadia tremor con-
821 strained by GPS, *J. Geophys. Res.*, *114*, B00A05, doi:10.1029/2008JB005909, 2009.
- 822 Ando, R., R. Nakata, and T. Hori, A slip pulse model with fault heterogeneity for low-
823 frequency earthquakes and tremor along plate interfaces, *Geophys. Res. Lett.*, *37*, L10310, doi:
824 10.1029/2010GL043056, 2010.
- 825 Ando, R., N. Takeda, and T. Yamashita, Propagation dynamics of seismic and aseismic slip gov-
826 erned by fault heterogeneity and Newtonian rheology, *J. Geophys. Res.*, *117*(B11), B11308,
827 doi:10.1029/2012JB009532, 2012.
- 828 Angiboust, S., J. Kirsch, O. Oncken, J. Glodny, P. Monié, and E. Rybacki, Probing the transition
829 between seismically coupled and decoupled segments along an ancient subduction interface,
830 *Geochem., Geophys., Geosyst.*, *16*(6), 1905–1922, doi:10.1002/2015GC005776, 2015.
- 831 Annoura, S., K. Obara, and T. Maeda, Total energy of deep low-frequency tremor in the
832 Nankai subduction zone, southwest Japan, *Geophys. Res. Lett.*, *43*(6), 2562–2567, doi:
833 10.1002/2016GL067780, 2016.
- 834 Ariyoshi, K., T. Hori, J.-P. Ampuero, Y. Kaneda, T. Matsuzawa, R. Hino, and A. Hasegawa,
835 Influence of interaction between small asperities on various types of slow earthquakes in
836 a 3-D simulation for a subduction plate boundary, *Gondwana Res.*, *16*(3-4), 534–544, doi:
837 10.1016/j.gr.2009.03.006, 2009.
- 838 Ariyoshi, K., T. Matsuzawa, J.-P. Ampuero, R. Nakata, T. Hori, Y. Kaneda, R. Hino, and
839 A. Hasegawa, Migration process of very low-frequency events based on a chain-reaction model
840 and its application to the detection of preseismic slip for megathrust earthquakes, *Earth Planets
841 Space*, *64*(8), 693–702, doi:10.5047/eps.2010.09.003, 2012.
- 842 Armbruster, J. G., W.-Y. Kim, and A. M. Rubin, Accurate tremor locations from coherent S and P
843 waves, *J. Geophys. Res.*, *119*(6), 5000–5013, doi:10.1002/2014JB011133, 2014.
- 844 Audet, P., and A. J. Schaeffer, Fluid pressure and shear zone development over the locked to slow
845 slip region in Cascadia, *Science Advances*, *4*(3), eaar2982, doi:10.1126/sciadv.aar2982, 2018.

- 846 Audet, P., M. G. Bostock, N. I. Christensen, and S. M. Peacock, Seismic evidence for over-
847 pressured subducted oceanic crust and megathrust fault sealing, *Nature*, 457, 76–78, doi:
848 10.1038/nature07650, 2009.
- 849 Baltay, A., G. Prieto, and G. C. Beroza, Radiated seismic energy from coda measurements
850 and no scaling in apparent stress with seismic moment, *J. Geophys. Res.*, 115, B08314, doi:
851 10.1029/2009JB006736, 2010.
- 852 Behr, W. M., A. J. Kotowski, and K. T. Ashley, Dehydration-induced rheological heterogene-
853 ity and the deep tremor source in warm subduction zones, *Geology*, 46(5), 475–478, doi:
854 10.1130/G40105.1, 2018.
- 855 Bell, R., R. Sutherland, D. H. N. Barker, S. Henrys, S. Bannister, L. Wallace, and J. Beavan,
856 Seismic reflection character of the Hikurangi subduction interface, New Zealand, in the region
857 of repeated Gisborne slow slip events, *Geophys. J. Intern.*, 180(1), 34–48, doi:10.1111/j.1365-
858 246X.2009.04401.x, 2010.
- 859 Ben-Zion, Y., Z. Peng, D. Okaya, L. Seeber, J. G. Armbruster, N. Ozer, A. J. Michael, S. Baris, and
860 M. Aktar, A shallow fault-zone structure illuminated by trapped waves in the Karadere–Duzce
861 branch of the North Anatolian Fault, western Turkey, *Geophys. J. Intern.*, 152(3), 699–717,
862 doi:10.1046/j.1365-246X.2003.01870.x, 2003.
- 863 Bilek, S. L., and E. R. Engdahl, Rupture characterization and aftershock relocations for the 1994
864 and 2006 tsunami earthquakes in the Java subduction zone, *Geophys. Res. Lett.*, 34(20), doi:
865 10.1029/2007GL031357, 2007.
- 866 Bilek, S. L., and T. Lay, Tsunami earthquakes possibly widespread manifestations of frictional
867 conditional stability, *Geophys. Res. Lett.*, 29(14), 1–4, doi:10.1029/2002GL015215, 2002.
- 868 Bostock, M. G., A. A. Royer, E. H. Hearn, and S. M. Peacock, Low frequency earthquakes
869 below southern Vancouver Island, *Geochem., Geophys., Geosyst.*, 13(11), Q11007, doi:
870 10.1029/2012GC004391, 2012.
- 871 Bostock, M. G., A. M. Thomas, G. Savard, L. Chuang, and A. M. Rubin, Magnitudes and moment-
872 duration scaling of low-frequency earthquakes beneath southern Vancouver Island, *J. Geophys.*
873 *Res.*, 120(9), 6329–6350, doi:10.1002/2015JB012195, 2015.
- 874 Bostock, M. G., A. M. Thomas, A. M. Rubin, and N. I. Christensen, On corner frequen-
875 cies, attenuation, and low-frequency earthquakes, *J. Geophys. Res.*, 122(1), 543–557, doi:
876 10.1002/2016JB013405, 2017.
- 877 Brown, J. R., G. C. Beroza, and D. R. Shelly, An autocorrelation method to detect low frequency
878 earthquakes within tremor, *Geophys. Res. Lett.*, 35(16), L16305, doi:10.1029/2008GL034560,
879 2008.
- 880 Brown, J. R., G. C. Beroza, S. Ide, K. Ohta, D. R. Shelly, S. Y. Schwartz, W. Rabbel, M. Thorwart,
881 and H. Kao, Deep low-frequency earthquakes in tremor localize to the plate interface in multiple
882 subduction zones, *Geophys. Res. Lett.*, 36, L19306, doi:10.1029/2009GL040027, 2009.

- 883 Cesca, S., T. Dahm, C. Juretzek, and D. Kühn, Rupture process of the 2001 May 7 Mw
884 4.3 Ekofisk induced earthquake, *Geophys. J. Intern.*, 187(1), 407–413, doi:10.1111/j.1365-
885 246X.2011.05151.x, 2011.
- 886 Chamberlain, C. J., D. R. Shelly, J. Townend, and T. A. Stern, Low-frequency earthquakes reveal
887 punctuated slow slip on the deep extent of the Alpine Fault, New Zealand, *Geochem., Geophys.,*
888 *Geosyst.*, 15(7), 2984–2999, doi:10.1002/2014GC005436, 2014.
- 889 Chestler, S. R., and K. C. Creager, Evidence for a scale-limited low-frequency earthquake source
890 process, *J. Geophys. Res.*, 122(4), 3099–3114, doi:10.1002/2016JB013717, 2017a.
- 891 Chestler, S. R., and K. C. Creager, A model for low-frequency earthquake slip, *Geochem., Geo-*
892 *phys., Geosyst.*, 18(12), 4690–4708, doi:10.1002/2017GC007253, 2017b.
- 893 Chounet, A., M. Vallée, M. Causse, and F. Courboux, Global catalog of earthquake rupture
894 velocities shows anticorrelation between stress drop and rupture velocity, *Tectonophysics*, 733,
895 148–158, doi:10.1016/j.tecto.2017.11.005, 2018.
- 896 Cochran, E. S., Y.-G. Li, P. M. Shearer, S. Barbot, Y. Fialko, and J. E. Vidale, Seismic and
897 geodetic evidence for extensive, long-lived fault damage zones, *Geology*, 37(4), 315–318, doi:
898 10.1130/G25306A.1, 2009.
- 899 Collettini, C., A. Niemeijer, C. Viti, S. A. Smith, and C. Marone, Fault structure, frictional prop-
900 erties and mixed-mode fault slip behavior, *Earth Planet. Sci. Lett.*, 311(3–4), 316–327, doi:
901 10.1016/j.epsl.2011.09.020, 2011.
- 902 Crotwell, H. P., T. J. Owens, and J. Ritsema, The TauP toolkit: flexible seismic travel-time and
903 ray-path utilities, *Seis. Res. Lett.*, 70(2), 154–160, doi:10.1785/gssrl.70.2.154, 1999.
- 904 DeDontney, N., E. L. Templeton-Barrett, J. R. Rice, and R. Dmowska, Influence of plastic de-
905 formation on bimaterial fault rupture directivity, *J. Geophys. Res.*, 116(B10), B10312, doi:
906 10.1029/2011JB008417, 2011.
- 907 Dunham, E. M., D. Belanger, L. Cong, and J. E. Kozdon, Earthquake ruptures with strongly rate-
908 weakening friction and off-fault plasticity, Part 1: Planar faults, *Bull. Seis. Soc. Amer.*, 101(5),
909 2296–2307, doi:10.1785/0120100075, 2011.
- 910 Eshelby, J. D., The determination of the elastic field of an ellipsoidal inclusion, and related prob-
911 lems, *Proc. Roy. Soc. London. Series A. Mathematical and Physical Sciences*, 241(1226), 376–
912 396, doi:10.1098/rspa.1957.0133, 1957.
- 913 Eshelby, J. D., The elastic field of a crack extending non-uniformly under general anti-plane
914 loading, *Journal of the Mechanics and Physics of Solids*, 17(3), 177–199, doi:16/0022-
915 5096(69)90032-5, 1969.
- 916 Fagereng, Å., and J. F. A. Diener, San Andreas Fault tremor and retrograde metamorphism, *Geo-*
917 *phys. Res. Lett.*, 38(23), L23303, doi:10.1029/2011GL049550, 2011.

- 918 Fagereng, Å., G. W. B. Hillary, and J. F. A. Diener, Brittle-viscous deformation, slow slip, and
919 tremor, *Geophys. Res. Lett.*, *41*(12), 4159–4167, doi:10.1002/2014GL060433, 2014.
- 920 Faulkner, D. R., T. M. Mitchell, J. Behnsen, T. Hirose, and T. Shimamoto, Stuck in the mud? Earth-
921 quake nucleation and propagation through accretionary forearcs, *Geophys. Res. Lett.*, *38*(18),
922 L18303, doi:10.1029/2011GL048552, 2011a.
- 923 Faulkner, D. R., T. M. Mitchell, E. Jensen, and J. Cembrano, Scaling of fault damage zones with
924 displacement and the implications for fault growth processes, *J. Geophys. Res.*, *116*, B05403,
925 doi:10.1029/2010JB007788, 2011b.
- 926 Fletcher, J. B., and A. McGarr, Moments, magnitudes, and radiated energies of non-volcanic
927 tremor near Cholame, CA, from ground motion spectra at UPSAR, *Geophys. Res. Lett.*, *38*(16),
928 L16314, doi:10.1029/2011GL048636, 2011.
- 929 Folesky, J., J. Kummerow, S. A. Shapiro, M. Häring, and H. Asanuma, Rupture directivity of fluid-
930 induced microseismic events: Observations from an enhanced geothermal system, *J. Geophys.*
931 *Res.*, *121*(11), 8034–8047, doi:10.1002/2016JB013078, 2016.
- 932 Fossum, A. F., and L. B. Freund, Nonuniformly moving shear crack model of a shallow focus
933 earthquake mechanism, *J. Geophys. Res.*, *80*(23), 3347, doi:10.1029/JB080i023p03343, 1975.
- 934 Frank, W. B., N. M. Shapiro, V. Kostoglodov, A. L. Husker, M. Campillo, J. S. Payero, and G. A.
935 Prieto, Low-frequency earthquakes in the Mexican Sweet Spot, *Geophys. Res. Lett.*, *40*(11),
936 2661–2666, doi:10.1002/grl.50561, 2013.
- 937 Frankel, A., High-frequency spectral falloff of earthquakes, fractal dimension of complex rup-
938 ture, b value, and the scaling of strength on faults, *J. Geophys. Res.*, *96*, 6291–6302, doi:
939 10.1029/91JB00237, 1991.
- 940 Fry, B., K. Chao, S. Bannister, Z. Peng, and L. Wallace, Deep tremor in New Zealand trig-
941 gered by the 2010 Mw8.8 Chile earthquake, *Geophys. Res. Lett.*, *38*(15), L15306, doi:
942 10.1029/2011GL048319, 2011.
- 943 Fusseis, F., M. R. Handy, and C. Schrank, Networking of shear zones at the brittle-to-viscous
944 transition (Cap de Creus, NE Spain), *Journal of Structural Geology*, *28*(7), 1228–1243, doi:
945 10.1016/j.jsg.2006.03.022, 2006.
- 946 Gao, H., D. A. Schmidt, and R. J. Weldon, Scaling relationships of source parameters for slow slip
947 events, *Bull. Seis. Soc. Amer.*, *102*(1), 352–360, doi:10.1785/0120110096, 2012.
- 948 Ghosh, A., J. E. Vidale, and K. C. Creager, Tremor asperities in the transition zone control evo-
949 lution of slow earthquakes, *J. Geophys. Res.*, *117*(B10), B10301, doi:10.1029/2012JB009249,
950 2012.
- 951 Gomberg, J., K. Creager, J. Sweet, J. Vidale, A. Ghosh, and A. Hotovec, Earthquake spectra and
952 near-source attenuation in the Cascadia subduction zone, *J. Geophys. Res.*, *117*(B5), B05312,
953 doi:10.1029/2011JB009055, 2012.

- 954 Got, J.-L., and J. Fréchet, Origins of amplitude variations in seismic doublets: Source or attenua-
955 tion process?, *Geophys. J. Intern.*, 114(2), 325–340, doi:10.1111/j.1365-246X.1993.tb03921.x,
956 1993.
- 957 Handy, M. R., G. Hirth, and R. Burgmann, Continental Fault Structure and Rheology from the
958 Frictional-to-Viscous Transition Downwards, in *Tectonic Faults: Agents of Change on a Dy-*
959 *namic Earth (Dahlem Workshop 95, Berlin, January 2005)*, edited by M. R. Handy, G. Hirth,
960 and N. Hovius, pp. 139–182, MIT Press, Cambridge, MA, 2007.
- 961 Hawthorne, J. C., and J.-P. Ampuero, A phase coherence approach to identifying co-located earth-
962 quakes and tremor, *Geophys. J. Intern.*, 209(2), 623–642, doi:10.1093/gji/ggx012, 2017.
- 963 Hawthorne, J. C., and N. M. Bartlow, Observing and modeling the spectrum of a slow slip event,
964 *J. Geophys. Res.*, 123(5), 4243–4265, doi:10.1029/2017JB015124, 2018.
- 965 Hawthorne, J. C., and A. M. Rubin, Laterally propagating slow slip events in a rate and state
966 friction model with a velocity-weakening to velocity-strengthening transition, *J. Geophys. Res.*,
967 118(7), 3785–3808, doi:10.1002/jgrb.50261, 2013.
- 968 Hayman, N. W., and L. L. Lavier, The geologic record of deep episodic tremor and slip, *Geology*,
969 42(3), 195–198, doi:10.1130/G34990.1, 2014.
- 970 Herrero, A., and P. Bernard, A kinematic self-similar rupture process for earthquakes, *Bull. Seis.*
971 *Soc. Amer.*, 84(4), 1216–1228, 1994.
- 972 Horowitz, F. G., and A. Ruina, Slip patterns in a spatially homogeneous fault model, *J. Geophys.*
973 *Res.*, 94(B8), 10,279–10,298, 1989.
- 974 Hough, S. E., Empirical Green’s function analysis: Taking the next step, *J. Geophys. Res.*, 102,
975 5369–5384, doi:10.1029/96JB03488, 1997.
- 976 Huang, Y., J.-P. Ampuero, and D. V. Helmberger, Earthquake ruptures modulated by waves in
977 damaged fault zones, *J. Geophys. Res.*, 119(4), 3133–3154, doi:10.1002/2013JB010724, 2014.
- 978 Ide, S., and S. Yabe, Universality of slow earthquakes in the very low frequency band, *Geophys.*
979 *Res. Lett.*, 41(8), 2786–2793, doi:10.1002/2014GL059712, 2014.
- 980 Ide, S., F. Imamura, Y. Yoshida, and K. Abe, Source characteristics of the Nicaraguan
981 Tsunami Earthquake of September 2, 1992, *Geophys. Res. Lett.*, 20(9), 863–866, doi:
982 10.1029/93GL00683, 1993.
- 983 Ide, S., G. C. Beroza, D. R. Shelly, and T. Uchide, A scaling law for slow earthquakes, *Nature*,
984 447(7140), 76–79, doi:10.1038/nature05780, 2007.
- 985 Ide, S., K. Imanishi, Y. Yoshida, G. C. Beroza, and D. R. Shelly, Bridging the gap between seis-
986 mically and geodetically detected slow earthquakes, *Geophys. Res. Lett.*, 35(10), L10305, doi:
987 10.1029/2008GL034014, 2008.

- 988 Ihmlé, P. F., J.-M. Gomez, P. Heinrich, and S. Guibourg, The 1996 Peru tsunamigenic earthquake:
989 Broadband source process, *Geophys. Res. Lett.*, 25(14), 2691–2694, doi:10.1029/98GL01987,
990 1998.
- 991 Kanamori, H., and E. E. Brodsky, The physics of earthquakes, *Reports on Progress in Physics*,
992 67(8), 1429–1496, doi:10.1088/0034-4885/67/8/R03, 2004.
- 993 Kanamori, H., and L. Rivera, Energy partitioning during an earthquake, *Washington DC American*
994 *Geophysical Union Geophysical Monograph Series*, 170, 3–13, doi:10.1029/170GM03, 2006.
- 995 Kane, D. L., P. M. Shearer, B. P. Goertz-Allmann, and F. L. Vernon, Rupture directivity of small
996 earthquakes at Parkfield, *J. Geophys. Res.*, 118(1), 212–221, doi:10.1029/2012JB009675, 2013.
- 997 Kano, M., A. Kato, R. Ando, and K. Obara, Strength of tremor patches along deep transition zone
998 of a megathrust, *Scientific Reports*, 8(1), 3655, doi:10.1038/s41598-018-22048-8, 2018.
- 999 Kato, A., Illuminating deep tremors along the Nankai subduction zone, Japan, by matched filter
1000 technique, *JpGU-AGU Joint Meeting*, pp. SSS04–02, 2017.
- 1001 Kato, A., T. Iidaka, R. Ikuta, Y. Yoshida, K. Katsumata, T. Iwasaki, S. Sakai, C. Thurber,
1002 N. Tsumura, K. Yamaoka, T. Watanabe, T. Kunitomo, F. Yamazaki, M. Okubo, S. Suzuki, and
1003 N. Hirata, Variations of fluid pressure within the subducting oceanic crust and slow earthquakes,
1004 *Geophys. Res. Lett.*, 37, L14310, doi:10.1029/2010GL043723, 2010.
- 1005 Kennett, B. L. N., and E. R. Engdahl, Traveltimes for global earthquake location and phase identi-
1006 fication, *Geophys. J. Intern.*, 105(2), 429–465, doi:10.1111/j.1365-246X.1991.tb06724.x, 1991.
- 1007 Kitajima, H., and D. M. Saffer, Elevated pore pressure and anomalously low stress in regions
1008 of low frequency earthquakes along the Nankai Trough subduction megathrust, *Geophys. Res.*
1009 *Lett.*, 39(23), L23301, doi:10.1029/2012GL053793, 2012.
- 1010 Kostrov, B. V., Unsteady propagation of longitudinal shear cracks, *Journal of Applied Mathematics*
1011 *and Mechanics*, 30(6), 1241–1248, doi:10.1016/0021-8928(66)90087-6, 1966.
- 1012 Kwiatek, G., K. Plenkers, G. Dresen, and J. R. Group, Source parameters of picoseismicity
1013 recorded at Mponeng deep gold mine, South Africa: implications for scaling relations, *Bull.*
1014 *Seis. Soc. Amer.*, 101(6), 2592–2608, doi:10.1785/0120110094, 2011.
- 1015 Langer, J. S., J. M. Carlson, C. R. Myers, and B. E. Shaw, Slip complexity in dynamic models
1016 of earthquake faults, *Proceedings of the National Academy of Sciences*, 93(9), 3825–3829, doi:
1017 10.1073/pnas.93.9.3825, 1996.
- 1018 Leclère, H., F. Cappa, D. Faulkner, O. Fabbri, P. Armitage, and O. Blake, Development and main-
1019 tenance of fluid overpressures in crustal fault zones by elastic compaction and implications for
1020 earthquake swarms, *J. Geophys. Res.*, 120(6), 4450–4473, doi:10.1002/2014JB011759, 2015.
- 1021 Lengliné, O., and J.-L. Got, Rupture directivity of microearthquake sequences near Parkfield, Cal-
1022 ifornia, *Geophys. Res. Lett.*, 38, L08310, doi:10.1029/2011GL047303, 2011.

- 1023 Lengliné, O., W. B. Frank, D. Marsan, and J. P. Ampuero, Imbricated slip rate processes during
1024 slow slip transients imaged by low-frequency earthquakes, *Earth Planet. Sci. Lett.*, 476, 122–
1025 131, doi:10.1016/j.epsl.2017.07.032, 2017.
- 1026 Lewis, M. A., and Y. Ben-Zion, Diversity of fault zone damage and trapping structures in the Park-
1027 field section of the San Andreas Fault from comprehensive analysis of near fault seismograms,
1028 *Geophys. J. Intern.*, 183(3), 1579–1595, doi:10.1111/j.1365-246X.2010.04816.x, 2010.
- 1029 Li, Y.-G., R. D. Catchings, and M. R. Goldman, Subsurface fault damage zone of the 2014 Mw
1030 6.0 South Napa, California, earthquake viewed from fault-zone trapped waves, *Bull. Seis. Soc.
1031 Amer.*, 106(6), 2747–2763, doi:10.1785/0120160039, 2016.
- 1032 Lin, G., C. H. Thurber, H. Zhang, E. Hauksson, P. M. Shearer, F. Waldhauser, T. M. Brocher, and
1033 J. Hardebeck, A California statewide three-dimensional seismic velocity model from both ab-
1034 solute and differential times, *Bull. Seis. Soc. Amer.*, 100(1), 225–240, doi:10.1785/0120090028,
1035 2010.
- 1036 Liu, L., M. Gurnis, M. Seton, J. Saleeby, R. D. Muller, and J. M. Jackson, The role of oceanic
1037 plateau subduction in the Laramide orogeny, *Nat. Geosci.*, 3(5), 353–357, doi:10.1038/ngeo829,
1038 2010.
- 1039 Liu, Y. J., and J. R. Rice, Aseismic slip transients emerge spontaneously in three-dimensional
1040 rate and state modeling of subduction earthquake sequences, *J. Geophys. Res.*, 110, B08307,
1041 doi:10.1029/2004JB003424, 2005.
- 1042 Liu, Y. J., and J. R. Rice, Spontaneous and triggered aseismic deformation transients in a subduc-
1043 tion fault model, *J. Geophys. Res.*, 112(B9), B09404, doi:10.1029/2007JB004930, 2007.
- 1044 Luo, Y., and J.-P. Ampuero, Tremor migration patterns and the collective behavior of deep asperi-
1045 ties mediated by creep, *EarthArXiv*, doi:10.17605/OSF.IO/MBCAV, 2017.
- 1046 Ma, S., A self-consistent mechanism for slow dynamic deformation and large tsunami genera-
1047 tion for earthquakes in the shallow subduction zone, *Geophys. Res. Lett.*, 39(11), L11310, doi:
1048 10.1029/2012GL051854, 2012.
- 1049 Madariaga, R., Seismic source theory, in *Treatise on Geophysics*, vol. 4: Earthquake Seismology,
1050 edited by H. Kanamori and G. Schubert, p. 6054, Elsevier, Amsterdam, 2007.
- 1051 Maeda, T., and K. Obara, Spatiotemporal distribution of seismic energy radiation from
1052 low-frequency tremor in western Shikoku, Japan, *J. Geophys. Res.*, 114, B00A09, doi:
1053 10.1029/2008JB006043, 2009.
- 1054 Mai, P. M., and G. C. Beroza, A spatial random field model to characterize complexity in earth-
1055 quake slip, *J. Geophys. Res.*, 107(B11), 2308, doi:10.1029/2001JB000588, 2002.
- 1056 McGuire, J. J., Estimating finite source properties of small earthquake ruptures, *Bull. Seis. Soc.
1057 Amer.*, 94(2), 377–393, doi:10.1785/0120030091, 2004.

- 1058 Melgar, D., and G. P. Hayes, Systematic observations of the slip pulse properties of large earth-
1059 quake ruptures, *Geophys. Res. Lett.*, *44*(19), 9691–9698, doi:10.1002/2017GL074916, 2017.
- 1060 Mori, J., and A. Frankel, Source parameters for small events associated with the 1986 North Palm
1061 Springs, California, earthquake determined using empirical Green functions, *Bull. Seis. Soc.*
1062 *Amer.*, *80*(2), 278–295, 1990.
- 1063 Mueller, C. S., Source pulse enhancement by deconvolution of an empirical Green's function,
1064 *Geophys. Res. Lett.*, *12*(1), 33–36, doi:10.1029/GL012i001p00033, 1985.
- 1065 Nakata, R., R. Ando, T. Hori, and S. Ide, Generation mechanism of slow earthquakes: Numerical
1066 analysis based on a dynamic model with brittle-ductile mixed fault heterogeneity, *J. Geophys.*
1067 *Res.*, *116*(B8), B08308, doi:10.1029/2010JB008188, 2011.
- 1068 Nowack, R. L., and M. G. Bostock, Scattered waves from low-frequency earthquakes and
1069 plate boundary structure in northern Cascadia, *Geophys. Res. Lett.*, *40*(16), 4238–4243, doi:
1070 10.1002/grl.50826, 2013.
- 1071 Obara, K., Nonvolcanic deep tremor associated with subduction in southwest Japan, *Science*,
1072 *296*(5573), 1679–1681, doi:10.1126/science.1070378, 2002.
- 1073 Ohta, K., and S. Ide, Precise hypocenter distribution of deep low-frequency earthquakes and its
1074 relationship to the local geometry of the subducting plate in the Nankai subduction zone, Japan,
1075 *J. Geophys. Res.*, *116*, B01308, doi:10.1029/2010JB007857, 2011.
- 1076 Payero, J. S., V. Kostoglodov, N. Shapiro, T. Mikumo, A. Iglesias, X. Perez-Campos, and R. W.
1077 Clayton, Nonvolcanic tremor observed in the Mexican subduction zone, *Geophys. Res. Lett.*, *35*,
1078 L07305, doi:10.1029/2007GL032877, 2008.
- 1079 Perfettini, H., and J. P. Ampuero, Dynamics of a velocity strengthening fault region: Im-
1080 plications for slow earthquakes and postseismic slip, *J. Geophys. Res.*, *113*, B09411, doi:
1081 10.1029/2007JB005398, 2008.
- 1082 Peterson, C. L., and D. H. Christensen, Possible relationship between nonvolcanic tremor and
1083 the 1998–2001 slow slip event, south central Alaska, *J. Geophys. Res.*, *114*, B06302, doi:
1084 10.1029/2008JB006096, 2009.
- 1085 Polet, J., and H. Kanamori, Tsunami earthquakes, in *Encyclopedia of complexity and systems*
1086 *science*, pp. 9577–9592, Springer, New York, 2009.
- 1087 Poulet, T., E. Veveakis, K. Regenauer-Lieb, and D. A. Yuen, Thermo-poro-mechanics of chemi-
1088 cally active creeping faults: 3. The role of serpentinite in episodic tremor and slip sequences, and
1089 transition to chaos, *J. Geophys. Res.*, *119*(6), 4606–4625, doi:10.1002/2014JB011004, 00001,
1090 2014.
- 1091 Prieto, G. A., P. M. Shearer, F. L. Vernon, and D. Kilb, Earthquake source scaling and self-
1092 similarity estimation from stacking P and S spectra, *J. Geophys. Res.*, *109*(B8), B08310, doi:
1093 10.1029/2004JB003084, 2004.

- 1094 Rempe, M., T. Mitchell, J. Renner, S. Nippres, Y. Ben-Zion, and T. Rockwell, Damage and seis-
1095 mic velocity structure of pulverized rocks near the San Andreas Fault, *J. Geophys. Res.*, 118(6),
1096 2813–2831, doi:10.1002/jgrb.50184, 2013.
- 1097 Rice, J. R., The mechanics of earthquake rupture, in *Physics of the Earth's Interior (Proc. Intl.*
1098 *School of Physics "E. Fermi" Course 78)*, edited by A. M. Dziewonski and E. Boschi, pp. 555–
1099 650, Italian Physical Society / North Holland Publishing Co., 1980.
- 1100 Rogers, G., and H. Dragert, Episodic tremor and slip on the Cascadia subduction zone: the chatter
1101 of silent slip, *Science*, 300(5627), 1942–1943, doi:10.1126/science.1084783, 2003.
- 1102 Roten, D., K. B. Olsen, and S. M. Day, Off-fault deformations and shallow slip deficit from dy-
1103 namic rupture simulations with fault zone plasticity, *Geophys. Res. Lett.*, 44(15), 7733–7742,
1104 doi:10.1002/2017GL074323, 2017.
- 1105 Rowe, C. D., F. Meneghini, and J. C. Moore, Fluid-rich damage zone of an ancient out-of-sequence
1106 thrust, Kodiak Islands, Alaska, *Tectonics*, 28, 1–20, doi:10.1029/2007TC002126, 2009.
- 1107 Royer, A. A., and M. G. Bostock, A comparative study of low frequency earthquake templates
1108 in northern Cascadia, *Earth Planet. Sci. Lett.*, 402, 247–256, doi:10.1016/j.epsl.2013.08.040,
1109 2014.
- 1110 Royer, A. A., A. M. Thomas, and M. G. Bostock, Tidal modulation and triggering of
1111 low-frequency earthquakes in northern Cascadia, *J. Geophys. Res.*, 120(1), 384–405, doi:
1112 10.1002/2014JB011430, 2015.
- 1113 Rubin, A. M., Episodic slow slip events and rate-and-state friction, *J. Geophys. Res.*, 113, B11414,
1114 doi:10.1029/2008JB005642, 2008.
- 1115 Rubin, A. M., Properties of Creep Fronts on Rate-and-State Faults, *Eos Trans. AGU, Fall Meeting*
1116 *Suppl.*, 21, T21F–08, 2009.
- 1117 Rubin, A. M., and J. G. Armbruster, Imaging slow slip fronts in Cascadia with high pre-
1118 cision cross-station tremor locations, *Geochem., Geophys., Geosyst.*, pp. 5371–5392, doi:
1119 10.1002/2013GC005031, 2013.
- 1120 Rubin, A. M., and M. G. Bostock, What is This Thing Called Tremor?, *Eos Trans. AGU, Fall*
1121 *Meeting Suppl.*, 52, 2017.
- 1122 Rubinstein, J. L., D. R. Shelly, and W. L. Ellsworth, Non-volcanic tremor: a window into the roots
1123 of fault zones, in *New Frontiers in Integrated Solid Earth Sciences*, edited by J. Negendank and
1124 S. Cloetingh, pp. 287–314, Springer, Dordrecht, 2009.
- 1125 Saffer, D. M., and L. M. Wallace, The frictional, hydrologic, metamorphic and thermal habitat of
1126 shallow slow earthquakes, *Nat. Geosci.*, 8(8), 594–600, doi:10.1038/ngeo2490, 2015.
- 1127 Savard, G., and M. G. Bostock, Detection and location of low-frequency earthquakes using cross-
1128 station correlation, *Bull. Seis. Soc. Amer.*, 105(4), 2128–2142, doi:10.1785/0120140301, 2015.

- 1129 Seekins, L. C., and J. Boatwright, Rupture directivity of moderate earthquakes in northern Califor-
1130 nia, *Bull. Seis. Soc. Amer.*, *100*(3), 1107–1119, doi:10.1785/0120090161, 2010.
- 1131 Segall, P., A. M. Rubin, A. M. Bradley, and J. R. Rice, Dilatant strengthening as a mechanism for
1132 slow slip events, *J. Geophys. Res.*, *115*, B12305, doi:10.1029/2010JB007449, 2010.
- 1133 Seno, T., and T. Yamasaki, Low-frequency tremors, intraslab and interplate earthquakes in South-
1134 west Japan-from a viewpoint of slab dehydration, *Geophys. Res. Lett.*, *30*(22), 1–4, doi:
1135 10.1029/2003GL018349, 2003.
- 1136 Shaw, B. E., and J. R. Rice, Existence of continuum complexity in the elastodynamics of repeated
1137 fault ruptures, *J. Geophys. Res.*, *105*(B10), 23,791–23,810, doi:10.1029/2000JB900203, 2000.
- 1138 Shearer, P., *Introduction to Seismology*, 2 ed., Cambridge University Press, Cambridge, UK, 2009.
- 1139 Shelly, D. R., Migrating tremors illuminate complex deformation beneath the seismogenic San
1140 Andreas fault, *Nature*, *463*(7281), 648–652, doi:10.1038/nature08755, 2010a.
- 1141 Shelly, D. R., Periodic, chaotic, and doubled earthquake recurrence intervals on the deep San
1142 Andreas Fault, *Science*, *328*(5984), 1385–1388, doi:10.1126/science.1189741, 2010b.
- 1143 Shelly, D. R., A 15 year catalog of more than 1 million low-frequency earthquakes: Tracking
1144 tremor and slip along the deep San Andreas Fault, *J. Geophys. Res.*, *122*(5), 3739–3753, doi:
1145 10.1002/2017JB014047, 2017.
- 1146 Shelly, D. R., and J. L. Hardebeck, Precise tremor source locations and amplitude variations
1147 along the lower-crustal central San Andreas Fault, *Geophys. Res. Lett.*, *37*, L14301, doi:
1148 10.1029/2010GL043672, 2010.
- 1149 Shelly, D. R., G. C. Beroza, S. Ide, and S. Nakamura, Low-frequency earthquakes in Shikoku,
1150 Japan, and their relationship to episodic tremor and slip, *Nature*, *442*(7099), 188–191, doi:
1151 10.1038/nature04931, 2006.
- 1152 Shelly, D. R., G. C. Beroza, and S. Ide, Non-volcanic tremor and low-frequency earthquake
1153 swarms, *Nature*, *446*(7133), 305–307, doi:10.1038/nature05666, 2007.
- 1154 Shelly, D. R., W. L. Ellsworth, T. Ryberg, C. Haberland, G. S. Fuis, J. Murphy, R. M. Nadeau,
1155 and R. Bürgmann, Precise location of San Andreas Fault tremors near Cholame, California
1156 using seismometer clusters: Slip on the deep extension of the fault?, *Geophys. Res. Lett.*, *36*(1),
1157 L01303, doi:10.1029/2008GL036367, 2009.
- 1158 Shibazaki, B., and Y. Iio, On the physical mechanism of silent slip events along the deeper part of
1159 the seismogenic zone, *Geophys. Res. Lett.*, *30*(9), 1–4, doi:10.1029/2003GL017047, 2003.
- 1160 Shibazaki, B., and T. Shimamoto, Modelling of short-interval silent slip events in deeper sub-
1161 duction interfaces considering the frictional properties at the unstable-stable transition regime,
1162 *Geophys. J. Intern.*, *171*(1), 191–205, doi:10.1111/j.1365-246X.2007.03434.x, 2007.

- 1163 Shipton, Z. K., and P. A. Cowie, Damage zone and slip-surface evolution over μm to km scales
1164 in high-porosity Navajo sandstone, Utah, *Journal of Structural Geology*, 23(12), 1825–1844,
1165 doi:10.1016/S0191-8141(01)00035-9, 2001.
- 1166 Skarbek, R. M., A. W. Rempel, and D. A. Schmidt, Geologic heterogeneity can produce aseismic
1167 slip transients, *Geophys. Res. Lett.*, 39(21), L21306, doi:10.1029/2012GL053762, 2012.
- 1168 Song, T.-R. A., D. V. Helmberger, M. R. Brudzinski, R. W. Clayton, P. Davis, X. Perez-Campos,
1169 and S. K. Singh, Subducting slab ultra-slow velocity layer coincident with silent earthquakes in
1170 southern Mexico, *Science*, 324(5926), 502–506, doi:10.1126/science.1167595, 2009.
- 1171 Stefano, R. D., C. Chiarabba, L. Chiaraluce, M. Cocco, P. D. Gori, D. Piccinini, and L. Val-
1172 oroso, Fault zone properties affecting the rupture evolution of the 2009 (Mw 6.1) L’Aquila
1173 earthquake (central Italy): Insights from seismic tomography, *Geophys. Res. Lett.*, 38, L10310,
1174 doi:10.1029/2011GL047365, 2011.
- 1175 Sweet, J. R., K. C. Creager, and H. Houston, A family of repeating low-frequency earthquakes
1176 at the downdip edge of tremor and slip, *Geochem., Geophys., Geosyst.*, 15(9), 3713–3721, doi:
1177 10.1002/2014GC005449, 2014.
- 1178 Taira, T., D. S. Dreger, and R. M. Nadeau, Rupture process for micro-earthquakes inferred from
1179 borehole seismic recordings, *International Journal of Earth Sciences*, 104(6), 1499–1510, doi:
1180 10.1007/s00531-015-1217-8, 2015.
- 1181 Thomas, A. M., G. C. Beroza, and D. R. Shelly, Constraints on the source parameters of low-
1182 frequency earthquakes on the San Andreas Fault, *Geophys. Res. Lett.*, 43(4), 1464–1471, doi:
1183 10.1002/2015GL067173, 2016.
- 1184 Thomas, A. M., N. M. Beeler, Q. Bletery, R. Burgmann, and D. R. Shelly, Using low-frequency
1185 earthquake families on the San Andreas Fault as deep creepmeters, *J. Geophys. Res.*, 123(1),
1186 457–475, doi:10.1002/2017JB014404, 2018.
- 1187 Thomson, D. J., Spectrum estimation and harmonic analysis, *Proc. IEEE*, 70(9), 1055–1096, doi:
1188 10.1109/PROC.1982.12433, 1982.
- 1189 Tinti, E., E. Fukuyama, A. Piatanesi, and M. Cocco, A kinematic source-time function compatible
1190 with earthquake dynamics, *Bull. Seis. Soc. Amer.*, 95(4), 1211–1223, doi:10.1785/0120040177,
1191 2005.
- 1192 Uchide, T., P. M. Shearer, and K. Imanishi, Stress drop variations among small earthquakes before
1193 the 2011 Tohoku-oki, Japan, earthquake and implications for the main shock, *J. Geophys. Res.*,
1194 119(9), 7164–7174, doi:10.1002/2014JB010943, 2014.
- 1195 Ujiie, K., H. Saishu, Å. Fagereng, N. Nishiyama, M. Otsubo, H. Masuyama, and H. Kagi, An
1196 explanation of episodic tremor and slow slip constrained by crack-seal veins and viscous shear
1197 in subduction mélange, *Geophys. Res. Lett.*, 45, 5371–5379, doi:10.1029/2018GL078374, 2018.

- 1198 van Avendonk, H. J. A., W. S. Holbrook, D. Lizarralde, M. M. Mora, S. Harder, A. D. Bul-
1199 lock, G. E. Alvarado, and C. J. Ramírez, Seismic evidence for fluids in fault zones on top of
1200 the subducting Cocos Plate beneath Costa Rica, *Geophys. J. Intern.*, 181(2), 997–1016, doi:
1201 10.1111/j.1365-246X.2010.04552.x, 2010.
- 1202 Veedu, D. M., and S. Barbot, The Parkfield tremors reveal slow and fast ruptures on the same
1203 asperity, *Nature*, 532, 361–365, doi:10.1038/nature17190, 2016.
- 1204 Velasco, A. A., C. J. Ammon, and T. Lay, Empirical green function deconvolution of broadband
1205 surface waves: Rupture directivity of the 1992 Landers, California (Mw = 7.3), earthquake, *Bull.*
1206 *Seis. Soc. Amer.*, 84(3), 735–750, 1994.
- 1207 Venkataraman, A., and H. Kanamori, Observational constraints on the fracture energy of subduc-
1208 tion zone earthquakes, *J. Geophys. Res.*, 109(B5), B05302, doi:10.1029/2003JB002549, 2004.
- 1209 Veveakis, E., T. Poulet, and S. Alevizos, Thermo-poro-mechanics of chemically active
1210 creeping faults: 2. Transient considerations, *J. Geophys. Res.*, 119(6), 4583–4605, doi:
1211 10.1002/2013JB010071, 2014.
- 1212 Waldhauser, F., Near-real-time double-difference event location using long-term seismic archives,
1213 with application to northern California, *Bull. Seis. Soc. Amer.*, 99(5), 2736–2748, doi:
1214 10.1785/0120080294, 2009.
- 1215 Walter, J. I., S. Y. Schwartz, J. M. Protti, and V. Gonzalez, Persistent tremor within the northern
1216 Costa Rica seismogenic zone, *Geophys. Res. Lett.*, 38, L01307, doi:10.1029/2010GL045586,
1217 2011.
- 1218 Wang, E., and A. M. Rubin, Rupture directivity of microearthquakes on the San Andreas
1219 Fault from spectral ratio inversion, *Geophys. J. Intern.*, 186(2), 852–866, doi:10.1111/j.1365-
1220 246X.2011.05087.x, 2011.
- 1221 Watanabe, T., Y. Hiramatsu, and K. Obara, Scaling relationship between the duration and the
1222 amplitude of non-volcanic deep low-frequency tremors, *Geophys. Res. Lett.*, 34(7), L07305,
1223 doi:10.1029/2007GL029391, 2007.
- 1224 Webber, S., S. Ellis, and Å. Fagereng, “Virtual shear box” experiments of stress and slip
1225 cycling within a subduction interface mélange, *Earth Planet. Sci. Lett.*, 488, 27–35, doi:
1226 10.1016/j.epsl.2018.01.035, 2018.
- 1227 Wech, A. G., and K. C. Creager, Cascadia tremor polarization evidence for plate interface slip,
1228 *Geophys. Res. Lett.*, 34(22), doi:10.1029/2007GL031167, 2007.
- 1229 Yabe, S., and S. Ide, Spatial distribution of seismic energy rate of tectonic tremors in subduction
1230 zones, *J. Geophys. Res.*, 119(11), 8171–8185, doi:10.1002/2014JB011383, 2014.
- 1231 Yabe, S., and S. Ide, Slip-behavior transitions of a heterogeneous linear fault, *J. Geophys. Res.*,
1232 122(1), 387–410, doi:10.1002/2016JB013132, 2017.

- 1233 Yabe, S., A. S. Baltay, S. Ide, and G. C. Beroza, Seismic-wave attenuation determined from
1234 tectonic tremor in multiple subduction zones seismic-wave attenuation determined from tec-
1235 tonic tremor in multiple subduction zones, *Bull. Seis. Soc. Amer.*, *104*(4), 2043–2059, doi:
1236 10.1785/0120140032, 2014.
- 1237 Yang, H., Z. Li, Z. Peng, Y. Ben-Zion, and F. Vernon, Low-velocity zones along the San Jacinto
1238 Fault, Southern California, from body waves recorded in dense linear arrays, *J. Geophys. Res.*,
1239 *119*(12), 8976–8990, doi:10.1002/2014JB011548, 2014.
- 1240 Ye, L., T. Lay, H. Kanamori, and L. Rivera, Rupture characteristics of major and great ($M_w \geq$
1241 7.0) megathrust earthquakes from 1990 to 2015: 1. Source parameter scaling relationships, *J.*
1242 *Geophys. Res.*, *121*(2), 826–844, doi:10.1002/2015JB012426, 2016.
- 1243 Zhang, J., P. Gerstoft, P. M. Shearer, H. Yao, J. E. Vidale, H. Houston, and A. Ghosh, Cascadia
1244 tremor spectra: Low corner frequencies and earthquake-like high-frequency falloff, *Geochem.*,
1245 *Geophys.*, *Geosyst.*, *12*(10), Q10007, doi:10.1029/2011GC003759, 2011.